Reviewed Preprint
v1 • November 18, 2025
Not revised

Reviewed Preprint
v2 • May 5, 2026
Revised by authors

For correspondence:
ntuwx@ntu.edu.cn
chengjing@wchscu.cn
liudongtom@gmail.com

* These authors contributed equally to this work

Competing interests: No competing interests declared

Funding: See page 32

Reviewing editor: Matthew W Kelley, National Institute on Deafness and Other Communication Disorders, United States

HSD17B7 is required for the function of sensory hair cells by regulating cholesterol synthesis

Yuqian Shen[1,*], Ziyang Wang[1,*], Xun Wang[1], Fuping Qian[2], Mingjun Zhong[3], Xin Wang[2] ✉, Jing Cheng[3] ✉, Dong Liu[1] ✉

[1]Co-innovation Center of Neuroregeneration, School of Life Sciences, Nantong Laboratory of Development and Diseases, Nantong University, Nantong, China • [2]Institute of Special Environmental Medicine, Nantong University, Nantong, China • [3]Institute of Rare Diseases, West China Hospital of Sichuan University, Chengdu, China

eLife Assessment

This study provides **valuable** data on the role of Hsd17b7, a gene involved in cholesterol biosynthesis, as a potential regulator of mechanosensory hair cell function. The authors used both zebrafish and the HEI cell line to examine the effects of deletion of Hsd17b7 on hair cell function and survival. While the study presents **convincing** evidence, the effect sizes observed across several experiments, including functional readouts such as the acoustic startle response, are modest, which raises questions about the biological significance of the proposed mechanism.

https://doi.org/10.7554/eLife.108108.2.sa3

Abstract

Cholesterol homeostasis is fundamental to cellular function, and its disruption underlies a wide range of human diseases. However, the contribution of cholesterol biosynthesis to auditory physiology remains poorly understood. HSD17B7 (17β-Hydroxysteroid dehydrogenase type 7) catalyzes the conversion of zymosterone to zymosterol, a key step in the post-lanosterol cholesterol biosynthetic pathway. Here, we found that Hsd17b7 is highly enriched in sensory hair cells of zebrafish and mice. The deficiency of Hsd17b7 deficiency reduced intracellular cholesterol levels in HEI-OC1 cells and zebrafish hair cells, thereby compromising MET and acoustic startle responses. A heterozygous nonsense variant (c.544G>T; p.E182*) in *HSD17B7* was identified in an individual with bilateral profound hearing loss. mRNA of c.544G>T HSD17B7 failed to rescue the impaired MET and acoustic startle response of hsd17b7 mutants. Mechanistically, the mutation decreases mRNA abundance and significantly reduces protein. Moreover, expression of the p.E182* mutation disrupted the interaction between HSD17B7 and the ER retention receptor RER1, leading to aberrant subcellular localization and altered cholesterol distribution, thereby exacerbating HC dysfunction. Together, our findings suggest a conserved and essential role for HSD17B7-mediated cholesterol biosynthesis in sensory hair cell function and identify HSD17B7 as a candidate gene for sensorineural hearing loss.

Introduction

Hearing loss is one of the most common sensory disorders worldwide and represents a major global health burden. According to the World Health Organization, more than 466 million people currently suffer from disabling hearing loss, and this number is expected to increase substantially in the coming decades [1]. Genetic factors account for approximately 60% of congenital hearing loss, and mutations in genes that regulate the development and function of sensory hair cells (HCs)

are the main cause of hereditary deafness. Although more than 150 non-syndromic deafness genes have been identified [2], the molecular mechanisms underlying HC dysfunction remain incompletely understood, and many pathogenic genes remain to be discovered.

HCs are the primary mechanoreceptors of the auditory and vestibular systems, converting mechanical stimuli into electrical signals through mechanotransduction (MET). This process critically depends on the integrity and biophysical properties of hair cell membranes, particularly those of the stereocilia. Cholesterol is the most abundant sterol molecule in mammalian cells and plays essential roles in maintaining membrane structure, synthesizing important hormones, facilitating synapse formation, and mediating cell signaling transduction [3–6]. Previous studies have shown that dysregulated intracellular cholesterol homeostasis contributes to auditory defects [6–8], including hereditary [9–13], noise-induced [14–16], ototoxic [17, 18], and age-related hearing loss [19–21]. HSD17B7 is a member of the hydroxysteroid dehydrogenase family and functions as a key enzyme in the cholesterol biosynthetic pathway by catalyzing the conversion of zymosterone to zymosterol. In addition to its role in steroid metabolism [22] and its involvement in hormone-related cancers [23, 24], HSD17B7 has been reported to be expressed in multiple tissues, including the brain, eye, and inner ear [25, 26]. Notably, single-cell RNA sequencing (scRNA-seq) and immunostaining analyses have suggested that HSD17B7 is enriched in mouse vestibular HCs [27]. Despite this expression pattern, the functional role of HSD17B7 in HCs and MET has not been investigated, and no pathogenic variants have been reported to be associated with hearing loss.

Here, our findings reveal a previously unrecognized link between hair cell–intrinsic cholesterol biosynthesis and the function of sensory hair cells, and identify HSD17B7 as a candidate gene underlying sensory hearing disorders.

Results

Hsd17b7 is expressed in sensory hair cells of zebrafish and mice

To assess the role of Hsd17b7 in the auditory system, we first investigated the expression of *hsd17b7* in the developing zebrafish. scRNA-seq data analysis (accession no. GSE221471) [28] categorized lateral line hair cells (LLHCs) (cluster 0), supporting cell (cluster 1), macula hair cells (MHCs) (cluster 2), crista hair cells (CHCs) 1 (cluster 3), mantle cell (cluster 4), and CHCs 2 (cluster 5) using the Seurat 4.0.1 platform (Figure 1A). The feature plot and violin plot showed that *hsd17b7* was expressed in sensory HCs, especially in LLHCs and CHCs (Figure 1B and C). Quantitative comparison of average expression levels within LLHCs indicates that *hsd17b7* is expressed at a level comparable to several known MET-associated genes (e.g., *tmc1* and *lhfpl5a*) (Figure 1D). To examine the temporal dynamics of *hsd17b7* expression during LLHCs differentiation, LLHCs, supporting cells, and mantle cells were ordered along pseudotime using Monocle 3 (Figure 1E). A heatmap was generated to visualize the expression dynamics of marker genes along the LLHC developmental trajectory (Figure 1F). These analyses suggested a gradual increase in *hsd17b7* expression during LLHC maturation (Figure 1E and F). Consistently, whole-mount *in situ* hybridization (WISH) further showed that *hsd17b7* was specifically enriched in neuromast and crista regions at 72 and 96 hours post-fertilization (hpf) (Figure 1G). To further explore the subcellular localization of *hsd17b7* in zebrafish HCs, we generated a *hsd17b7-egfp* fusion construct driven by a HC-specific *myo6b* promoter [29, 30]. Confocal imaging revealed that hsd17b7-EGFP localized predominantly to the cytoplasm in both CHCs and LLHCs, exhibiting a punctate distribution pattern (Figure 1H and I).

To further elucidate Hsd17b7 expression in the mammalian auditory system, we analyzed three published scRNA-seq datasets from mouse inner ear tissues [31–33]. These analyses revealed that Hsd17b7 was enriched in sensory hair cells, including outer hair cells (OHCs), inner hair cells (IHCs), and utricular hair cells (UHCs), while lower expression levels were observed in CHCs (Figure 1J). Next, we performed immunostaining to assess Hsd17b7 protein expression in the organ of Corti. Hsd17b7 was detected in both OHCs and IHCs at P1, P4, and P7 (Figure 1K). The

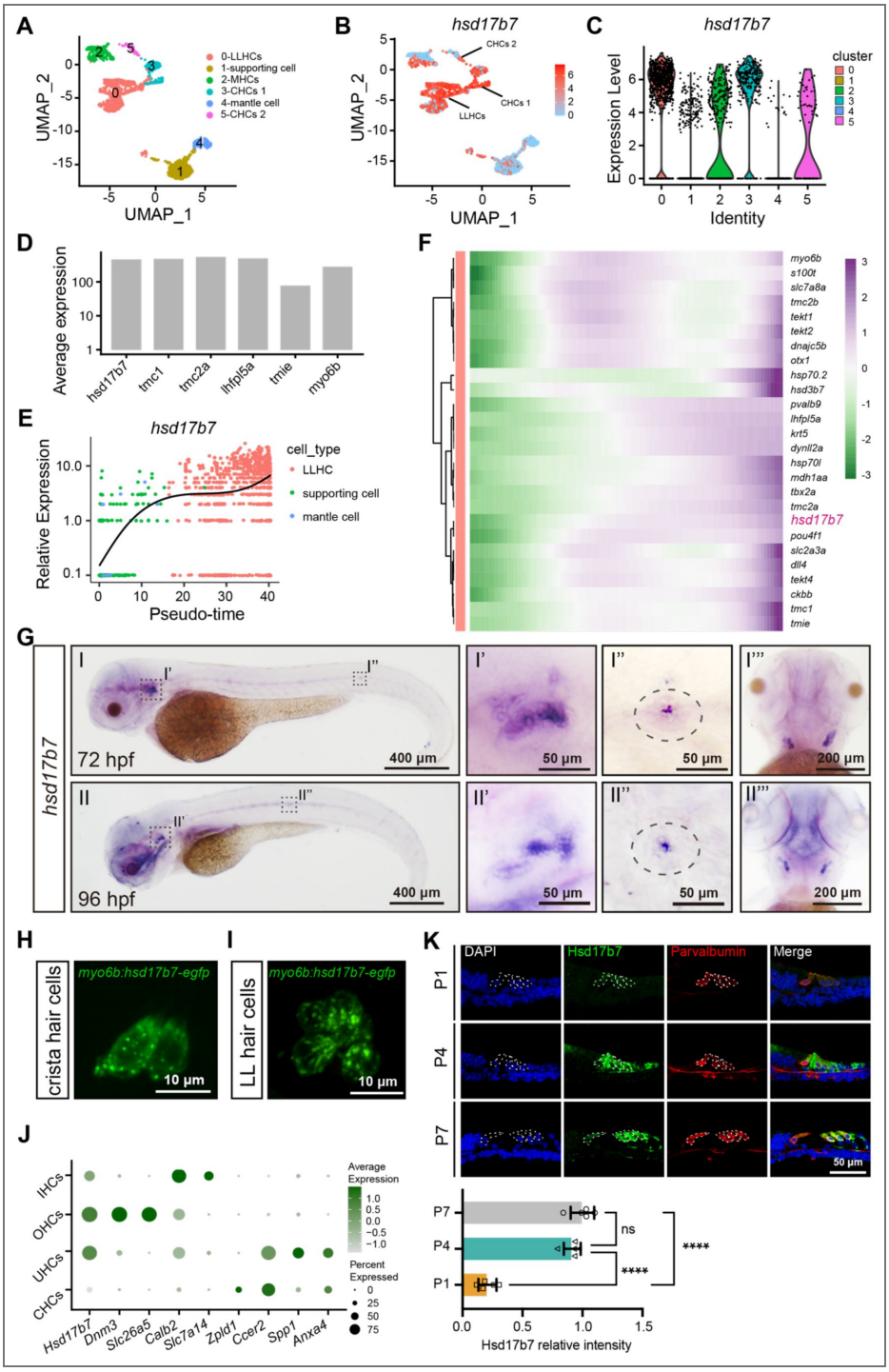

Figure 1. Conserved expression of *Hsd17b7* in zebrafish and mice sensory hair cells.

(A) The UMAP analysis of the zebrafish scRNA-seq data. LLHCs, lateral line hair cells; MHCs, macula hair cells; CHCs, crista hair cells; (B, C) Feature plot and violin plot of *hsd17b7* expression across cell types. (D) Quantitative comparison of average expression levels of hsd17b7 within LLHCs. (E) *hsd17b7* expression increased along the pseudotime trajectory of LLHC formation. (F) Heatmap of marker genes along the pseudotime trajectory. (G) The expression of the *hsd17b7* in 72 hpf and 96 hpf embryos was detected by whole-mount *in situ* hybridization analysis. Dashed circles indicate the otic vesicle and the neuromast. (H, I) Representative images of the CHCs and LLHCs in *Tg(myo6b: hsd17b7-egfp)* at 4 dpf. (J) The average expression of Hsd17b7 and HC marker genes across mouse HC subtypes from published scRNA-seq datasets. UHCs, utricular hair cells. (K) Immunostaining and quantification analysis of HSD17B7 in dissected mouse organ of Corti sections at P1, P4, and P7. Dashed circles indicate outer hair cells (OHCs) and inner hair cells (IHCs).

specificity of the Hsd17b7 antibody was further supported by independent validation experiments in HEI-OC1 cells (Figure S1A and B). These results indicate that Hsd17b7 is expressed and enriched in HCs in both zebrafish and mice.

In addition, phylogenetic and sequence alignment analysis revealed that vertebrate HSD17B7s share a significant similarity in amino acid sequences (Figure S2A). UniProt sequence alignment analysis revealed that *Danio rerio* hsd17b7 (NP_001070796.1) shares 58.2% identity with *Homo sapiens* HSD17B7 (NP_057455.1) and 67.1% identity with *Mus musculus* Hsd17b7 (NP_034606.3), respectively (Figure S2B). These data suggest that Hsd17b7 is conserved and expressed in HCs across vertebrate species.

Hsd17b7 deficiency impaired acoustic startle responses and MET activity in zebrafish

To investigate the *hsd17b7* function in the auditory system, we generated *hsd17b7* mutant alleles using CRISPR/Cas9-mediated genome editing (Figure S3A–D). Sequence analysis identified multiple mutant alleles, including a 4-bp deletion and two 6-bp deletions in exon 3 (Figure S3E). The 4-bp deletion allele was selected for further analysis, as it led to a frameshift and premature stop codon, producing a severely truncated protein lacking most of the conserved catalytic domain required for *hsd17b7* enzymatic activity (Figure S3F).

We first examined acoustic startle responses [34] at 5 dpf (Figure 2A). Compared with control larvae, *hsd17b7* mutants exhibited significantly reduced movement trajectories, peak swimming velocity, and total travel distance following acoustic stimulation (Figure 2A–C), indicating impaired startle response. Microinjection of *hsd17b7* mRNA into mutant embryos significantly restored these behavioral phenotypes (Figure 2A–C), confirming that the phenotype was specifically caused by loss of Hsd17b7.

To validate these findings, antisense morpholino oligonucleotides (*hsd17b7* Mo) targeting the junction of exon 1/intron 1 were designed to knock down hsd17b7 expression (Figure S4A and B). RT-PCR and immunoblotting analyses confirmed effective disruption of normal splicing and a substantial reduction in Hsd17b7 protein levels, both of which were rescued by co-injection of *hsd17b7* mRNA (Figure S4C and D). Consistent with the mutant phenotype, *hsd17b7* morphants displayed significantly reduced acoustic startle responses at 5 dpf, including decreased movement trajectories, swimming distance, and peak velocity, all of which were effectively rescued by *hsd17b7* mRNA injection (Figure S4E–G).

In the *Tg(Brn3c: mGFP)* background [28, 35], confocal imaging revealed a significant reduction in the number of LLHCs in *hsd17b7* mutants (~16% reduction) (Figure 2D and E). To assess whether *hsd17b7* loss affects the MET activity, we performed FM4-64 uptake assays, which label HCs through functional MET channels [26, 32, 33]. Quantification of FM4-64 fluorescence intensity per HC revealed a pronounced reduction in MET-dependent dye uptake in *hsd17b7* mutant HCs at 5 dpf (~40%; Figure 2F and G). A similar decrease was observed in *hsd17b7* morphants (~25%; Figure S5A and B). Importantly, *hsd17b7* mRNA injection restored both FM4-64 uptake and HC number in mutants and morphants (Figure 2D–G, Figure S5A and B), indicating that *hsd17b7* is required for normal MET activity in HCs.

Hsd17b7 deficiency disrupted cholesterol-associated transcriptional programs in hair cells

To investigate intrinsic transcriptional changes in HCs caused by hsd17b7 deficiency, we performed scRNA-seq on FACS-isolated $mGFP^+$ HCs from control and *hsd17b7* mutant (Figure 3A). Clustering analysis identified major inner ear (IE) and lateral line (LL) cell populations, including HCs and SCs (Figure 3B; Figure S6 A and B). Focusing on LLHCs, pseudobulk differential expression analysis revealed extensive transcriptional remodeling in *hsd17b7* mutants, with 1355 genes differentially expressed, including 853 upregulated (63%) and 502 downregulated (37%) genes relative to controls (Figure 3C). Gene Ontology enrichment analysis

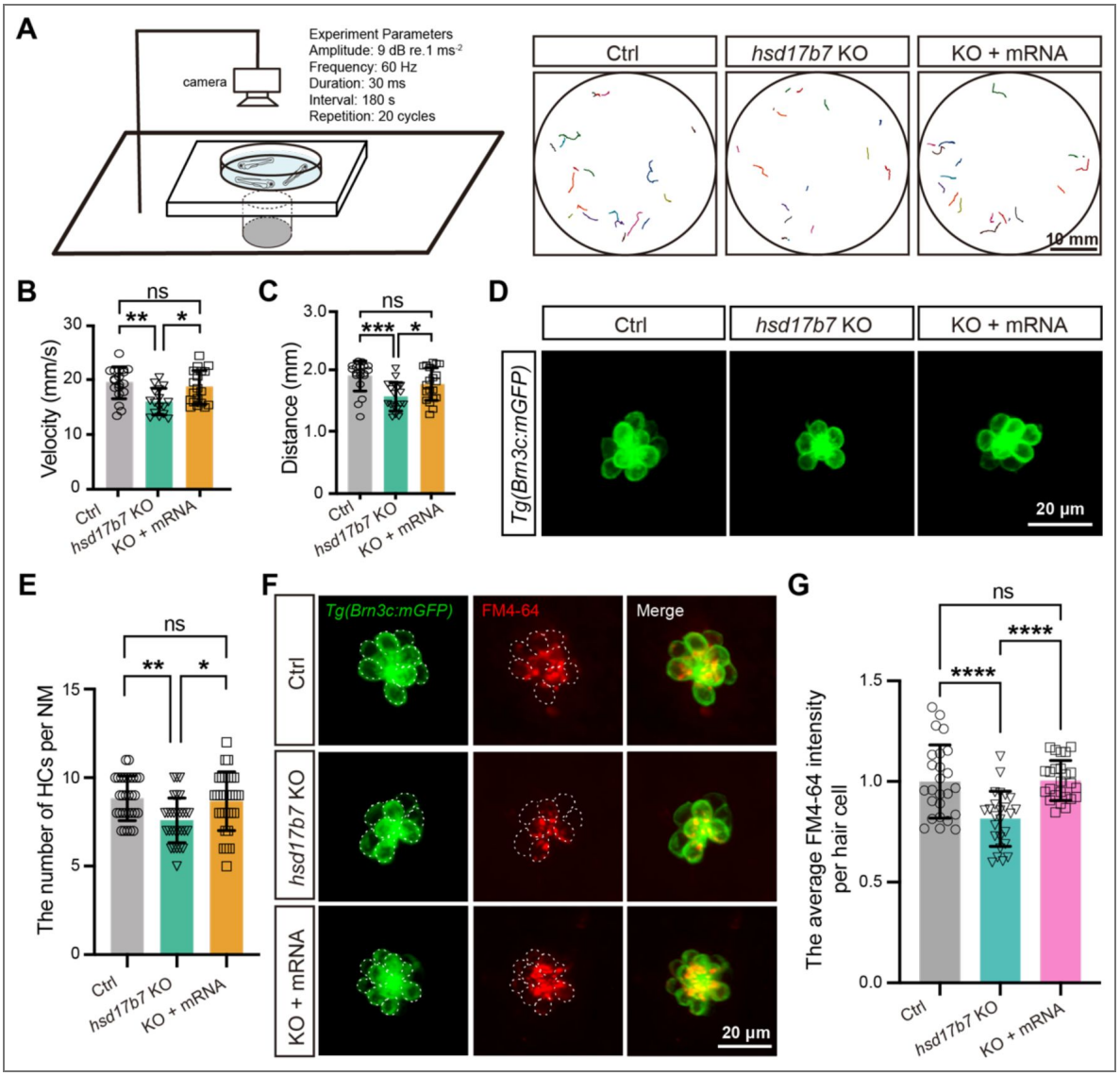

Figure 2. Loss of hsd17b7 impaired acoustic startle responses and mechanotransduction activity in zebrafish.

(A) Left, schematic of the experimental setup used to assess acoustic startle responses in zebrafish larvae. Right, representative locomotor trajectories showing C-start responses to a single acoustic stimulus (9 dB re. 1 $m \cdot s^{-2}$, 60 Hz tone burst) in control, *hsd17b7* knockout (KO), and *hsd17b7* mRNA–rescued larvae at 5 dpf. Scale bars, 10 mm. (B, C) Quantification of peak swimming velocity (B) and total movement distance (C) in response to acoustic stimulation shown in (A) (n = 20). One-way ANOVA followed by Tukey's multiple comparisons, $*P < 0.05$, $**P < 0.01$, $***P < 0.001$, ns, non-significant ($p > 0.05$), mean ± SEM. (D) Representative confocal images of lateral line hair cells (LLHCs, green) in *Tg(Brn3c:mGFP)* larvae at 4 dpf from control, *hsd17b7* KO, and *hsd17b7* mRNA–rescued groups. Scale bars, 20 μm. (E) Quantification of HC number per neuromast (n = 30). One-way ANOVA followed by Tukey's multiple comparisons, $*P < 0.05$, $**P < 0.01$, ns, non-significant ($p > 0.05$), mean ± SD. (F) Representative images of LLHCs (green) and FM4-64–labeled functional HCs (red) in single neuromasts of Tg(Brn3c:mGFP) larvae at 5 dpf from the indicated groups. White dashed outlines indicate LLHCs. Scale bars, 20 μm. (G) Quantification of relative FM4-64 fluorescence intensity per neuromast (n = 25). One-way ANOVA followed by Tukey's multiple comparisons, $****P < 0.0001$, ns, non-significant ($p > 0.05$), mean ± SD.

of differentially expressed genes highlighted pathways related to lipid metabolism, membrane organization, and sensory perception, indicating broad alterations in cellular homeostasis upon disruption of cholesterol biosynthesis (Figure 3D and E).

To further assess cholesterol- and MET-associated transcriptional programs, we performed module score analysis in both LLHCs and IEHCs. In mutant IEHCs, MET, cholesterol biosynthesis, and cholesterol uptake-related gene sets were significantly upregulated, whereas gene modules associated with tip-link components and cholesterol efflux were concurrently reduced (Figure 3F and G).

In mutant LLHCs, module score analysis revealed a partially overlapping transcriptional response. Gene modules associated with tip-link components and cholesterol efflux were reduced, whereas modules representing the core MET machinery and cholesterol biosynthesis enzymes did not show significant global changes, consistent with selective remodeling rather than uniform pathway activation or repression. At the gene level, cholesterol regulatory programs appeared partially uncoupled, with downregulation of sterol-sensing transcriptional regulators (e.g., *srebf2*, *insig1*, and *mbtps1*) accompanied by variable expression changes among cholesterol biosynthetic enzymes. In line with this pattern, gene set enrichment analysis (GSEA) indicated an overall attenuation of cholesterol biosynthesis–associated pathways in mutant LLHCs (Figure 3H).

Together, these findings indicate that *hsd17b7* deficiency induces selective and context-dependent remodeling of cholesterol- and MET-associated transcriptional programs across HC populations.

Hsd17b7 is required for maintaining cholesterol levels in hair cells

Hsd17b7 converts zymosterone to zymosterol, participating in cholesterol biosynthesis (Figure 4A) [26]. Given that both elevated and reduced cholesterol levels are detrimental to auditory function [7, 36], we first verified whether hsd17b7 regulates cholesterol homeostasis in hair cells.

In vitro, knockdown of *Hsd17b7* in HEI-OC1 cells resulted in a significant reduction in total cellular cholesterol levels (Figure 4B and C). To further examine cholesterol distribution, we employed the D4H cholesterol-binding probe derived from perfringolysin O, which selectively labels cholesterol at the cytoplasmic leaflet of the plasma membrane [37, 38]. Overexpression of human *HSD17B7* markedly increased D4H-mCherry fluorescence intensity in HEI-OC1 cells compared with controls (Figure 4D and E), indicating that HSD17B7 positively regulates cellular cholesterol abundance.

To further assess whether *hsd17b7* regulates cholesterol *in vivo*, we expressed D4H-mCherry in control and *hsd17b7* mutant zebrafish hair cells using the *Tg(Brn3c:mGFP)* background (Figure 4F). Consistent with previous reports [37], D4H-mCherry was enriched in the hair bundle (Figure 4G). Notably, cholesterol levels, as indicated by D4H-mCherry intensity, were significantly reduced in both CHCs and LLHCs of *hsd17b7* mutants at 4 dpf (Figure 4G and H). A comparable reduction was observed in *hsd17b7* morphants (Figure S5C–F).

Together, these results demonstrate that *hsd17b7* is required for maintaining cholesterol levels in HCs, both *in vitro* and *in vivo*. Given the essential role of cholesterol homeostasis in MET and auditory function [7,36,39], loss of Hsd17b7 likely compromises MET activity and acoustic startle responses by disrupting cholesterol availability in HCs.

Identification of a candidate HSD17B7 nonsense variant associated with hearing loss

Given the established role of Hsd17b7 in HCs, we investigated whether variants in the human *HSD17B7* might be associated with hearing loss. Whole-genome sequencing (WGS) was performed in individuals with hearing loss who remained undiagnosed after screening of 201 known deafness-associated genes [39]. We identified a heterozygous nonsense variant in *HSD17B7* (NM_016371.4), c.544G>T (p.E182*), in a child with bilateral profound congenital hearing loss (Figure 5A–C). The proband failed the newborn hearing screening, required special education during early childhood, and was diagnosed with bilateral profound hearing loss by 8 years of age. Physical examination revealed two preauricular appendages anterior to the right ear, without

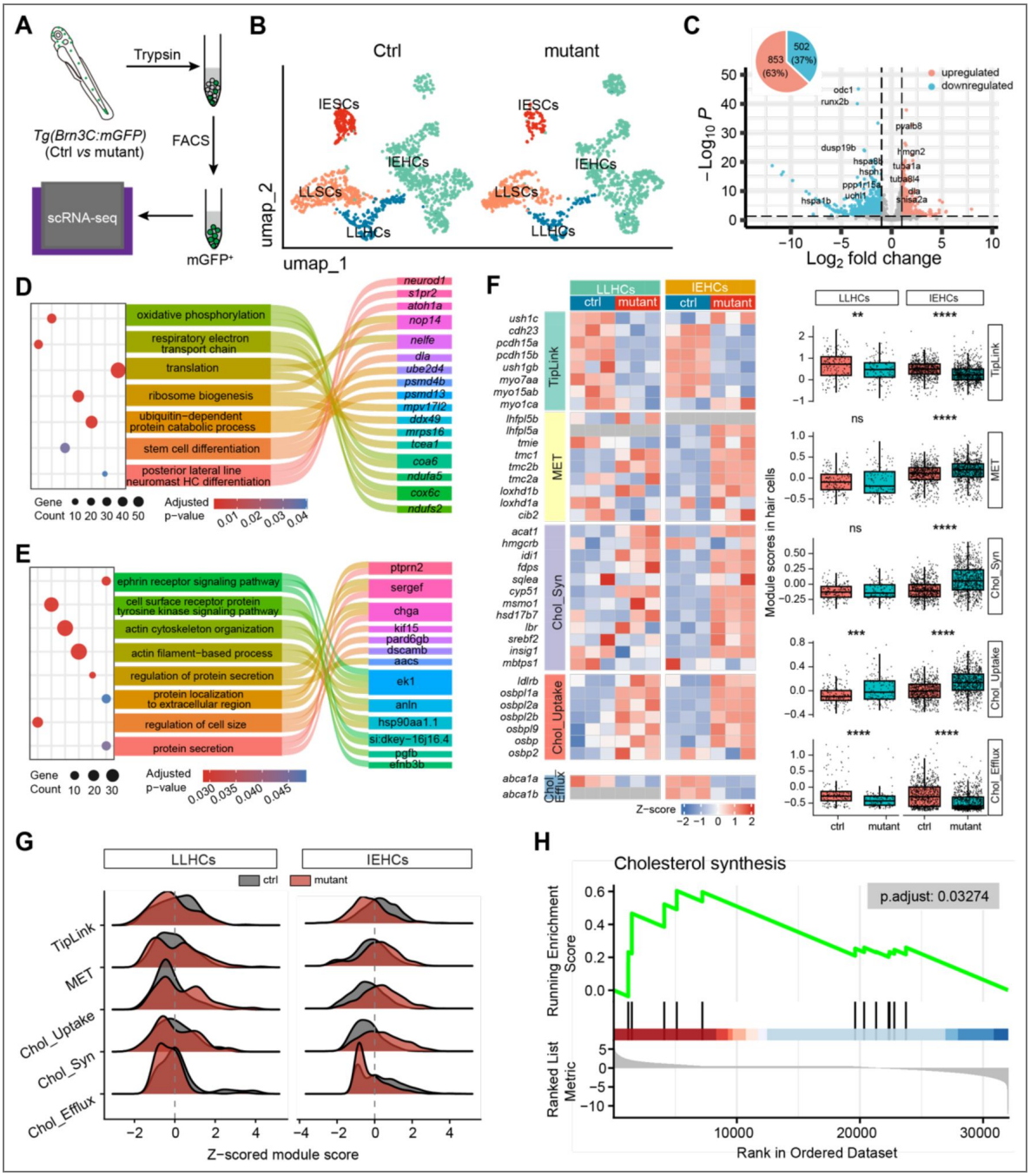

Figure 3. Hsd17b7 deficiency disrupted cholesterol-associated transcriptional states in hair cells.

(A) Schematic overview of the scRNA-seq workflow. mGFP^{+} hair cells were isolated from control and hsd17b7 mutant zebrafish by fluorescence-activated cell sorting (FACS) and subjected to 10× Genomics single-cell RNA sequencing. (B) UMAP visualization of scRNA-seq data from control and hsd17b7 mutant samples, colored by annotated cell types, including inner ear (IE) and lateral line (LL) hair cells (HCs) and supporting cells (SCs). (C) Volcano plot showing pseudobulk differential gene expression analysis of LLHCs from hsd17b7 mutants relative to controls. Genes with adjusted $p < 0.05$ are highlighted, with upregulated genes shown in red and downregulated genes shown in blue. (D and E) Gene Ontology (GO) biological process enrichment analysis of genes upregulated and downregulated in hsd17b7 mutant HCs. A Sankey diagram illustrates representative genes contributing to each enriched GO term. (F) Heatmap and module score analysis of gene sets related to tip-link structure, mechanotransduction (MET), and cholesterol metabolism in LLHCs and IEHCs. Module scores were calculated using predefined gene sets, and statistical significance was assessed using the Wilcoxon rank-sum test. (G) Ridge plots showing the distribution of z-scored module scores associated with tip link structure, cholesterol uptake, and cholesterol efflux in control and hsd17b7 mutant LLHCs and IEHCs, revealing population-wide transcriptional shifts rather than discrete subpopulation changes. (H) Gene set enrichment analysis (GSEA) demonstrating significant downregulation of cholesterol biosynthesis–associated pathways in hsd17b7 mutant LLHCs.

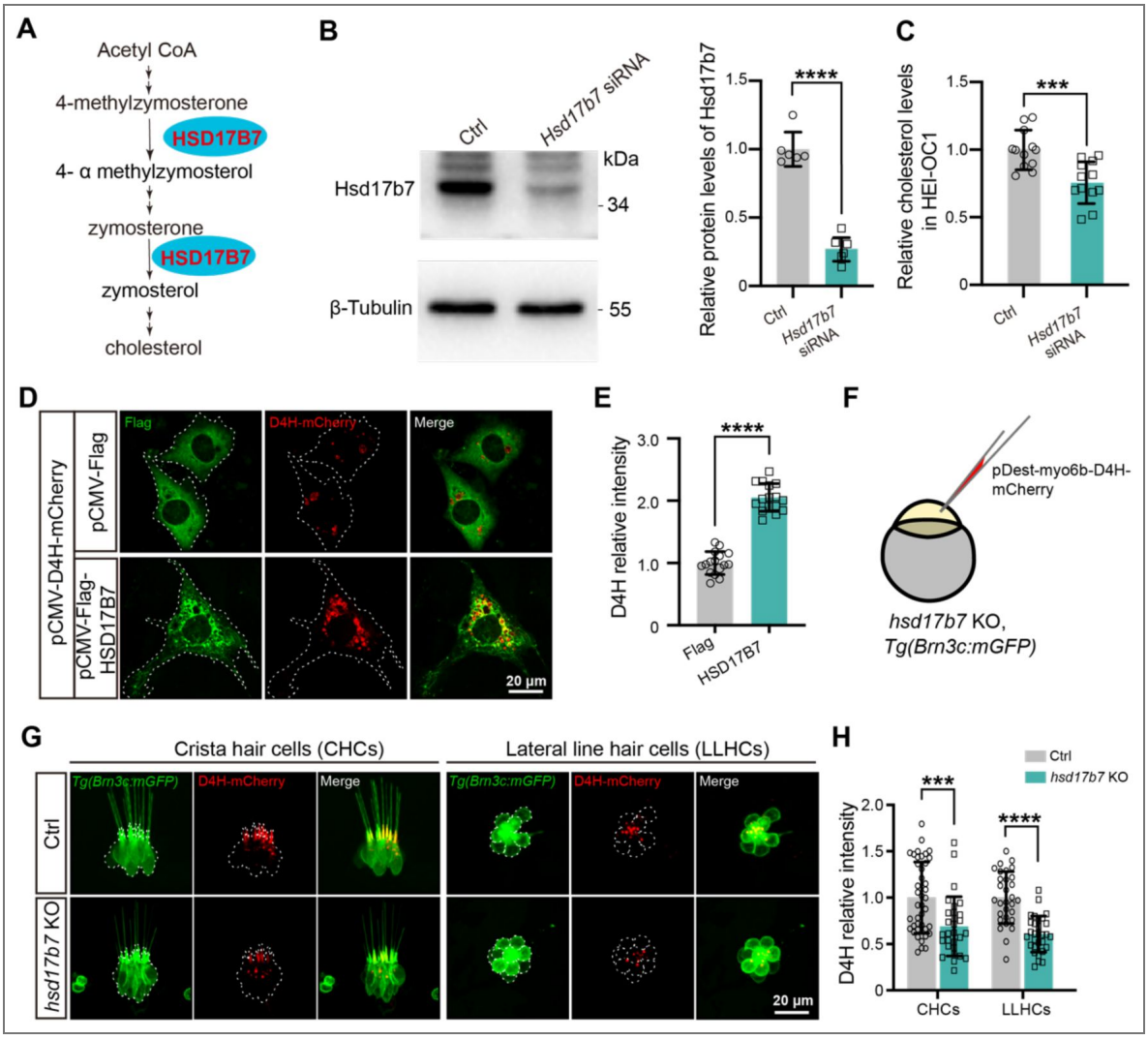

Figure 4. Hsd17b7 deficiency reduced cholesterol in hair cells.

(A) Schematic illustration of the cholesterol biosynthesis pathway highlighting the role of HSD17B7. (B) Western blot analysis of Hsd17b7 protein levels in control and *Hsd17b7*-knockdown HEI-OC1 cells; quantification is shown on the right (n = 6). Significance was determined by an unpaired two-tailed Student's *t*-test. ****$P < 0.0001$, mean ± SD. (C) Quantification of the relative cellular cholesterol levels in control and Hsd17b7-knockdown HEI-OC1 cells (n=12). Significance was determined by an unpaired two-tailed Student's *t*-test. ***$P < 0.001$, mean ± SD. (D) Representative immunofluorescence images showing the cholesterol probe D4H-mCherry in HEI-OC1 cells transfected with pCMV-Flag or pCMV-Flag–HSD17B7 plasmids. White dashed outlines indicate transfected cells. Scale bars, 20 μm. (E) Quantification of relative D4H-mCherry fluorescence intensity for (D) (n = 16). Significance was determined by an unpaired two-tailed Student's *t*-test. ****$P < 0.0001$, mean ± SD. (F) Experimental schematic illustrating expression of D4H-mCherry in control and *hsd17b7* knockout zebrafish larvae using the *Tg(Brn3c:mGFP)* background. (G) Representative confocal images of D4H-mCherry (red) in crista hair cells (CHCs) and lateral line hair cells (LLHCs) of control and *hsd17b7* knockout larvae at 4 dpf. White dashed outlines indicate hair cells. Scale bars, 20 μm. (H) Quantification of relative D4H-mCherry fluorescence intensity in vivo for (G) (n = 30). Significance was determined by an unpaired two-tailed Student's *t*-test. ***$P < 0.001$, ****$P < 0.0001$, mean ± SD.

additional systemic abnormalities. The proband Ⅱ 1's parents had normal hearing and no family history of hearing loss, but declined genetic testing, precluding segregation analysis (Figure 5A and B).

The p.E182* variant introduces a premature stop codon at position Glu182, resulting in a truncated HSD17B7 protein (Figure 5C). The multiple sequence alignment showed that Glu182 is evolutionarily conserved across vertebrates, from zebrafish to humans (Figure 5D). According to UniProt annotation, HSD17B7 contains an extracellular domain (1-229 aa), a transmembrane region (230-250 aa), and a cytoplasmic domain (251-341 aa). The p.E182* variant is predicted to remove the transmembrane region and cytoplasmic domain (Figure 5E). Together, these analyses identify p.E182* as a candidate variant in HSD17B7 that may be associated with hearing loss.

The HSD17B7^{E182*} truncation failed to rescue MET activity and auditory-related behaviors in hsd17b7 mutants

To assess the functional impact of the p.E182* variant, human HSD17B7 or truncation (HSD17B7^{E182*}) mRNAs were microinjected into the fertilized one-cell stage embryos of *hsd17b7* mutants. Injection of HSD17B7 mRNA significantly increased the FM4-64 uptake in LLHCs of *hsd17b7* mutants, whereas the injection of HSD17B7^{E182*} mRNA failed to restore FM4-64 labeling (Figure 6A and B), indicating that the truncated protein is unable to rescue normal MET activity. Consistently, acoustic startle response assays revealed that HSD17B7 mRNA rescued behavioral responses of hsd17b7 mutants, as assessed by movement trajectory, swimming distance, and peak velocity. In contrast, the p.E182* variant showed no rescuing effect on these behavioral deficits (Figure 6C–E).

The HSD17B7^{E182*} truncation disrupts intracellular cholesterol distribution and MET activity

To explore the potential contribution of HSD17B7^{E182*} truncation to the patient's hearing loss, we compared the cellular activation of the wild-type and truncated HSD17B7 *in vitro* and *vivo*. We analyzed the subcellular localization of Flag-tagged HSD17B7 and HSD17B7^{E182*} in HEI-OC1 cells. Since cholesterol synthesis mainly occurs in the endoplasmic reticulum (ER) [40, 41], HSD17B7 was expected to localize to this compartment. Consistent with this expectation, immunostaining in HEI-OC1 cells showed that Flag-tagged HSD17B7 co-localized with the ER marker Calnexin. In contrast, HSD17B7^{E182*} failed to localize to the ER and instead displayed a spot-like aggregate distribution (Figure 7A), a pattern further supported by fluorescence intensity profile analyses (Figure 7B and C).

Given that the patient is heterozygous for the variant, we next examined whether HSD17B7^{E182*} interferes with HSD17B7 subcellular localization. Co-expression of Flag-HSD17B7 and HSD17B7^{E182*}-Myc in HEI-OC1 cells showed that HSD17B7 retained its ER localization, indicating that the truncated protein does not significantly alter the subcellular distribution of the wild-type protein (Figure 7D and E).

To further investigate the function of HSD17B7^{E182*} expression *in vivo*, we overexpressed human HSD17B7 or HSD17B7^{E182*} in zebrafish HCs. The FM4-64 uptake assay revealed that the overexpression of HSD17B7 did not significantly affect FM4-64 fluorescence intensity in LLHCs compared to the control. In contrast, the expression of HSD17B7^{E182*} led to a significant reduction of fluorescence intensity (Figure 8A and B). Consistently, startle response assays showed that HSD17B7 overexpression showed comparable movement trajectories, distance, and velocity in response to auditory stimulation, whereas larvae expressing HSD17B7^{E182*} reduced startle-associated behaviors (Figure 8C-E). These data suggest that expression of HSD17B7^{E182*} negatively impacts auditory-related behavior *in vivo*.

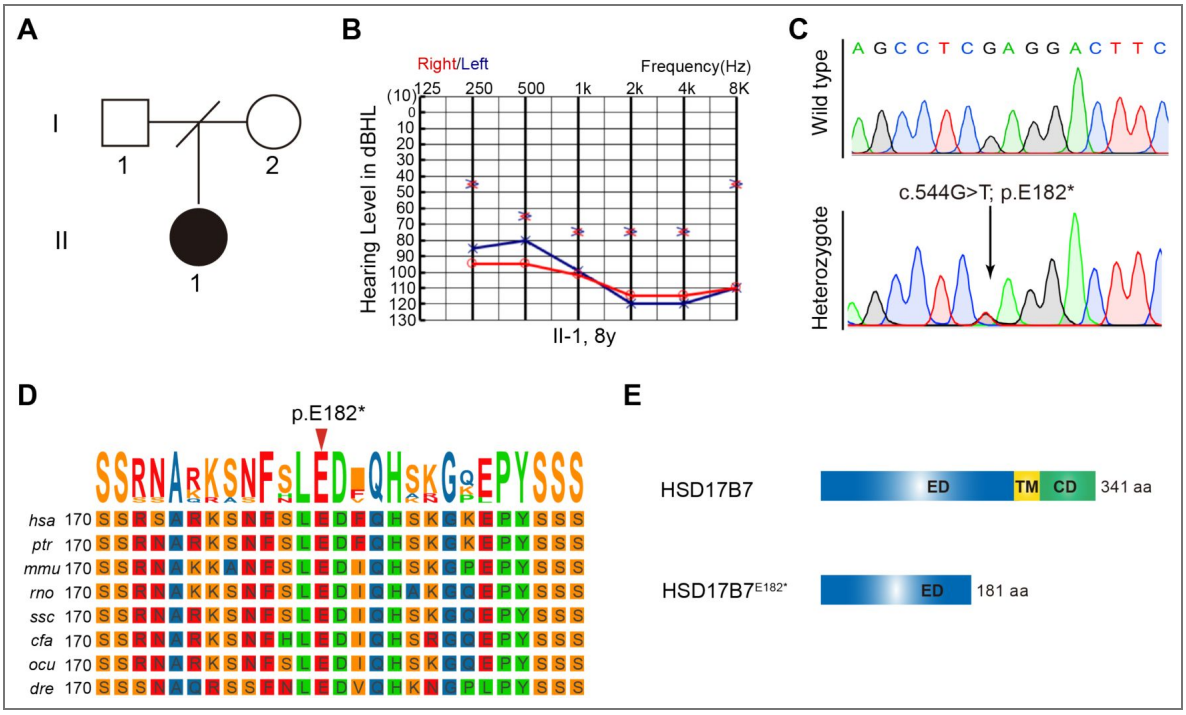

Figure 5. Identification of a heterozygous nonsense variant in human *HSD17B7*.

(A) Two-generation family pedigree for the affected individual. The hearing-impaired individual is indicated by a black circle (female). (B) Pure-tone audiometry audiograms for the hearing-impaired individual at 8 years old. Blue represents the results for the left ear and red for the right ear. The affected individual shows severe-to-profound or profound HI. (C) Sequence of HSD17B7 mRNA in wild type and heterozygote. (D) Multiple sequence alignment of 8 different species using the TBtools program. The p.Glu182 residue, as indicated by a red arrow, is evolutionarily conserved from zebrafish to human. (E) The domain structure of human HSD17B7 and HSD17B7^{E182*}. ED, extracellular domain; TM, transmembrane; CD, cytoplasmic domain. The residue numbers are labeled at right.

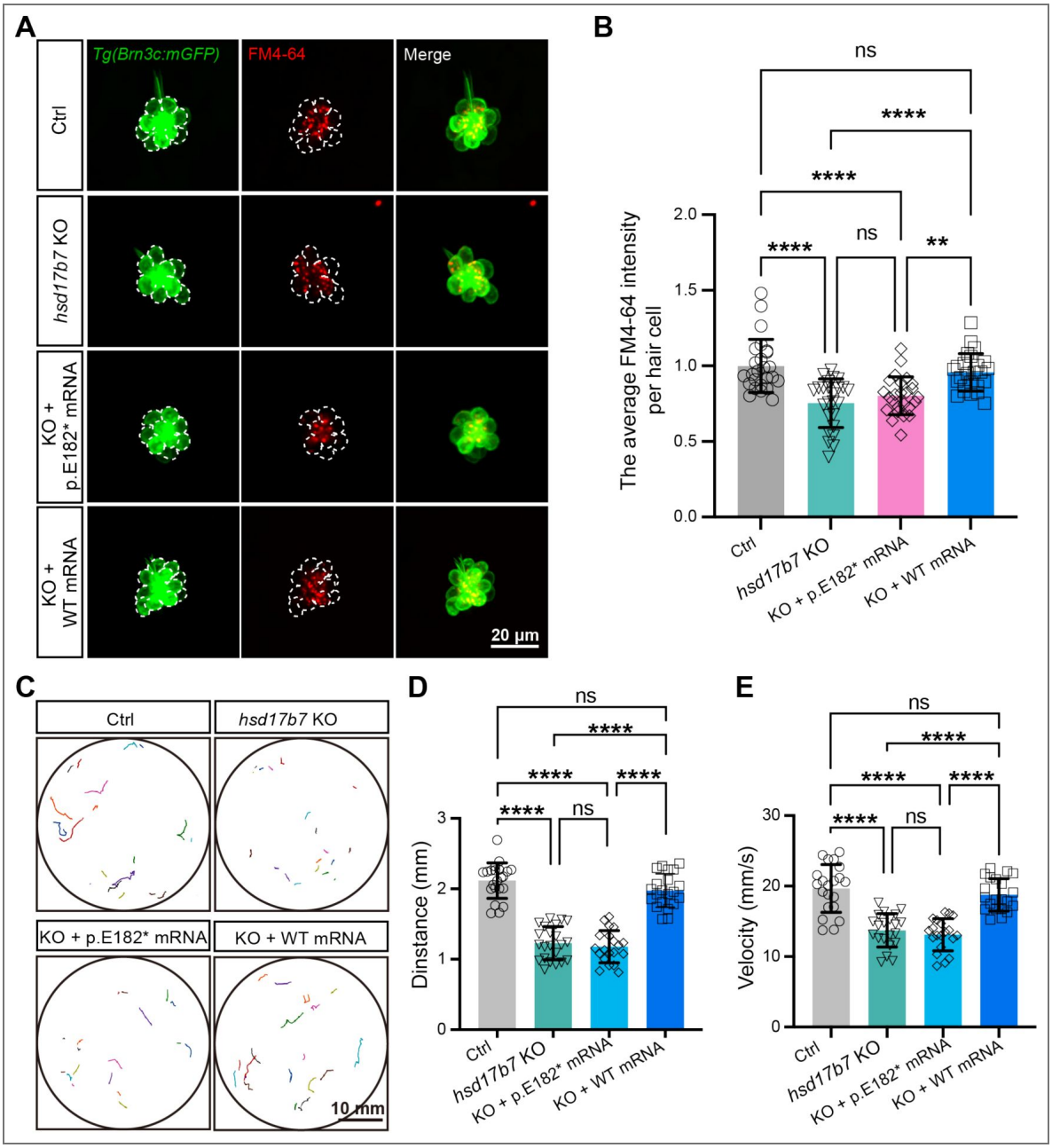

Figure 6. Wild-type but not HSD17B7^{E182*} restored MET activity and startle responses in hsd17b7 mutants.

(A) Representative images of lateral line hair cells (LLHCs, green) and FM4-64–labeled functional HCs (red) in single neuromasts of *Tg(Brn3c:mGFP)* at 5 dpf from control, *hsd17b7* knockout (KO), KO injected with *HSD17B7*^{E182*} (p.E182*) mRNA, and KO injected with *HSD17B7* (WT) mRNA groups. White dashed outlines indicate LLHCs. (B) Quantification of the relative FM4-64 intensity per HC (n=25). One-way ANOVA followed by Tukey's multiple comparisons, $^{**}P < 0.01$, $^{****}P < 0.0001$, ns, non-significant ($p > 0.05$), mean ± SD. (C) Representative locomotor trajectories of 5 dpf larvae exhibiting behavioral responses to a single acoustic stimulus (9 dB re. 1 m·s^{-2}, 60 Hz tone burst) in the indicated groups. (D, E) Quantification of total movement distance (D) and peak swimming velocity (E) in response to acoustic stimulation (n = 20). One-way ANOVA followed by Tukey's multiple comparisons, $^{****}P < 0.0001$, ns, non-significant ($p > 0.05$), mean ± SEM.

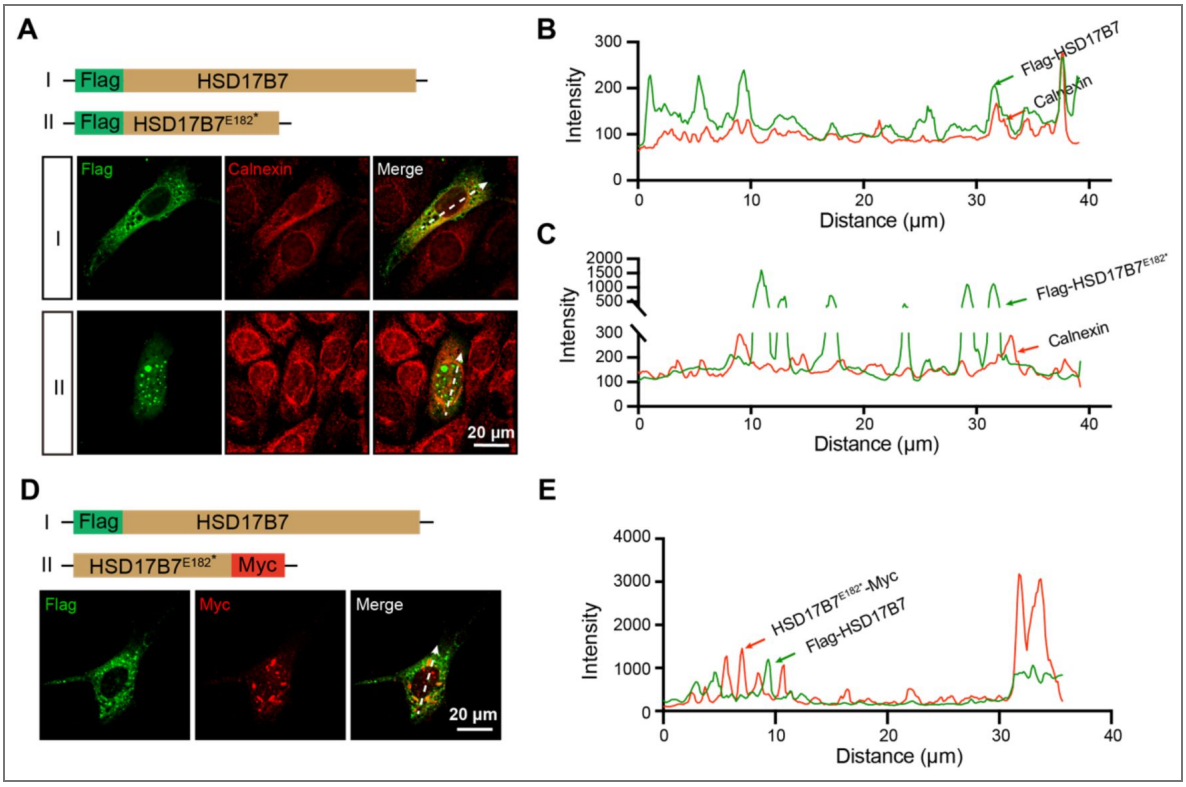

Figure 7. Subcellular localization of wild-type and p.E182* mutation HSD17B7.

(A) Immunostaining shows the subcellular localization of Flag-HSD17B7 and Flag-HSD17B7^{E182*} in HEI-OC1 cells. Calnexin was used as an endoplasmic reticulum (ER) marker. White arrows indicate the line-scan positions used for intensity profile analysis in (B) and (C). Scale bars, 20 μm. (B, C) Line-scan intensity profiles showing the spatial distribution of HSD17B7 (B) or HSD17B7^{E182*} (C) relative to the ER marker Calnexin along the indicated axes in (A). (D) Representative immunofluorescence image of a HEI-OC1 cell co-expressing HSD17B7 and HSD17B7^{E182*}. White arrows indicate the positions used for line-scan analysis. Scale bars, 20 μm. (E) Line-scan intensity profiles showing the intracellular distribution of HSD17B7 and HSD17B7^{E182*} along the indicated axis in (D).

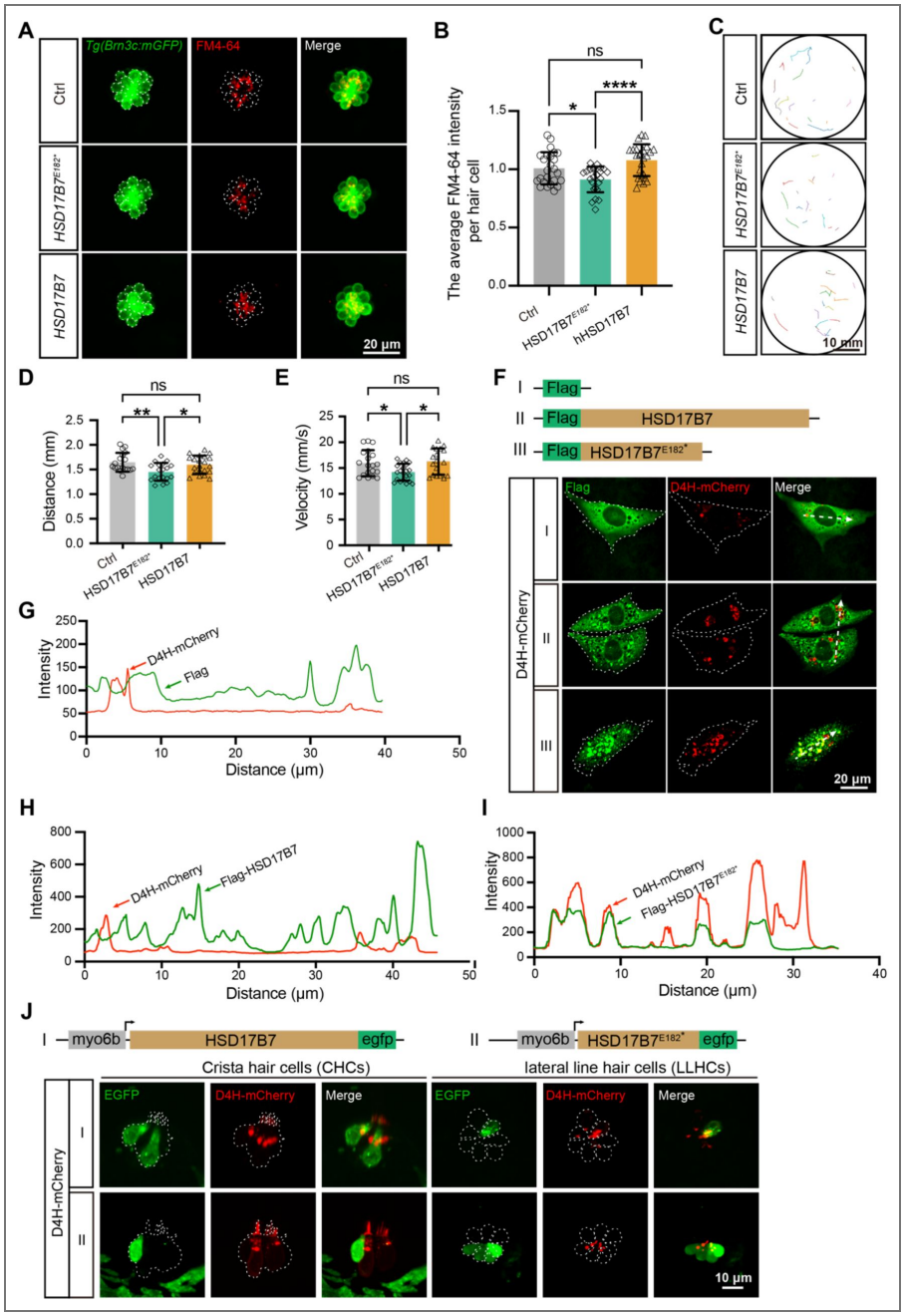

Figure 8. Expression of HSD17B7^{E182*} impaired mechanotransduction activity, auditory-related behavior, and cholesterol organization.

(A) Representative images of lateral line hair cells (LLHCs, green) and FM4-64–labeled functional hair cells (red) in single neuromasts of *Tg(Brn3c:mGFP)* larvae at 5 dpf following injection of HSD17B7 or HSD17B7^{E182*} mRNA. The white dashed indicates LLHCs. Scale bars, 20 μm. (B) Quantification of the FM4-64 relative intensity per LLHCs (n=25). One-way ANOVA followed by Tukey's multiple comparisons, *P < 0.05, ****P < 0.0001, ns, non-significant (p > 0.05), mean ± SD. (C-E) Moving traces and quantification of 20 embryos were filmed in 150 frames before and after stimulation (9 dB re. 1 m·s^{-2}, 60 Hz tone burst). Scale bars, 10 mm. One-way ANOVA followed by Tukey's multiple comparisons, *P < 0.05, **P < 0.01, ns, non-significant (p > 0.05), mean ± SEM. (F) Immunostaining of the cholesterol probe D4H in HEI-OC1 cells transfected with pCMV-Flag, pCMV-Flag-HSD17B7, and pCMV-Flag-HSD17B7^{E182*} constructs, respectively. White dashed outlines indicate transfected cells; arrows denote line-scan positions used for intensity profile analysis. Scale bars, 20 μm. (G–I) Line-scan intensity profiles showing the spatial distribution of Flag, HSD17B7, or HSD17B7^{E182*} relative to D4H signal along the indicated axes in (F). (J) Representative images of crista and lateral line hair cells in *Tg(myo6b: D4H-mCherry)* larvae following expression of myo6b-driven HSD17B7-EGFP or HSD17B7^{E182*}-EGFP at 4 dpf. White dashed outlines indicate HCs. Scale bars, 10 μm.

Given our findings that Hsd17b7 regulates cholesterol homeostasis (Figure 4) and previous research that proper cholesterol distribution is critical for HC function [37], we next examined whether the HSD17B7^{E182*} truncation disrupts intracellular cholesterol organization. HEI-OC1 cells were co-transfected with cholesterol probe D4H-mCherry together with pCMV-Flag, pCMV-Flag-HSD17B7, or pCMV-Flag-HSD17B7^{E182*}. While cholesterol distribution appeared as a diffuse pattern around the nucleus in the control and HSD17B7-expressing cells, HSD17B7^{E182*} resulted in a spot-like aggregation of D4H-mCherry (Figure 8F). Line-scan intensity analysis further confirmed the aberrant colocalization of HSD17B7^{E182*} with cholesterol-enriched compartments (Figure 8G-I).

To validate these observations in vivo, HSD17B7 or HSD17B7^{E182*} was expressed in zebrafish HCs by injecting pDest-myo6b-HSD17B7-EGFP or pDest-myo6b-HSD17B7^{E182*}-EGFP plasmids into the *Tg(myo6b: D4H-mCherry)* transgenic line (Figure 8J). In HCs expressing HSD17B7, the protein exhibited a punctate intracellular distribution and did not noticeably alter the D4H-mCherry cholesterol signal compared with neighboring non-expressing hair cells. In contrast, HSD17B7^{E182*} showed a diffuse localization throughout the cytoplasm and nucleus, accompanied by a marked reduction or near-complete loss of the D4H-mCherry signal in the stereocilia position. These data suggest that HSD17B7^{E182*} with aberrant subcellular localization may bind cholesterol and alter its intracellular distribution. Altogether, these results demonstrate that HSD17B7^{E182*} has a negative effect by altering cholesterol distribution in HCs, thereby compromising MET function and impaired startle responses.

HSD17B7^{E182*} truncation disrupted the interaction with RER1

To further explore the pathological consequences of HSD17B7^{E182*}, we compared the interaction landscapes of wild-type and mutant in HEI-OC1 cells (Figure 9A). Proteomic analysis of co-immunoprecipitated complexes revealed distinct interaction profiles between HSD17B7 and HSD17B7^{E182*} (Figure 9A–C; Figure S7). Proteins uniquely associated with HSD17B7 were strongly enriched for cholesterol metabolic processes, whereas those preferentially associated with HSD17B7^{E182*} were enriched for chromatin remodeling–related pathways.

Consistent with their subcellular localizations, cellular component analysis showed that HSD17B7-interacting proteins were predominantly enriched in the endoplasmic reticulum (ER), whereas HSD17B7^{E182*}-associated proteins were enriched in the nucleus and cytoplasm (Figure 9D), in agreement with immunostaining results (Figure 7A–C). Among ER-associated interactors, RER1 emerged as the top HSD17B7-specific binding partner (Figure 9E). RER1 is known to mediate ER retention of membrane-associated proteins [42, 43]. Direct binding between HSD17B7 and RER1 was confirmed by in *vitro* binding assays, whereas the HSD17B7^{E182*} failed to interact with RER1 (Figure 9F). Immunofluorescence analysis further demonstrated robust co-localization of RER1 with HSD17B7 but not with HSD17B7^{E182*} (Figure 9G–I), indicating that the p.E182* mutation disrupts RER1-mediated ER retention. Given that HSD17B7 is normally localized to the ER, loss of RER1 interaction provides a mechanistic explanation for the aberrant subcellular distribution of the mutant protein.

In addition to altered localization, the p.E182* mutation markedly reduced HSD17B7 expression levels. Compared with HSD17B7, the mutant protein exhibited substantially decreased abundance, accompanied by a significant reduction in mRNA levels (Figure S8A– C). mRNA stability assays revealed a shortened half-life of HSD17B7^{E182*} transcripts relative to wild-type (Figure S8D and E), indicating that the nonsense mutation compromises transcript stability and consequently reduces protein expression.

Discussion

This study reveals that HSD17B7 is enriched in sensory hair cells in zebrafish and mice. Using the zebrafish model, we show that loss of *hsd17b7* markedly reduces cholesterol levels in hair cells, leading to impaired MET function and abnormal hearing behaviors. These findings identify HSD17B7 as a previously unrecognized regulator of hair cell physiology and a candidate gene for

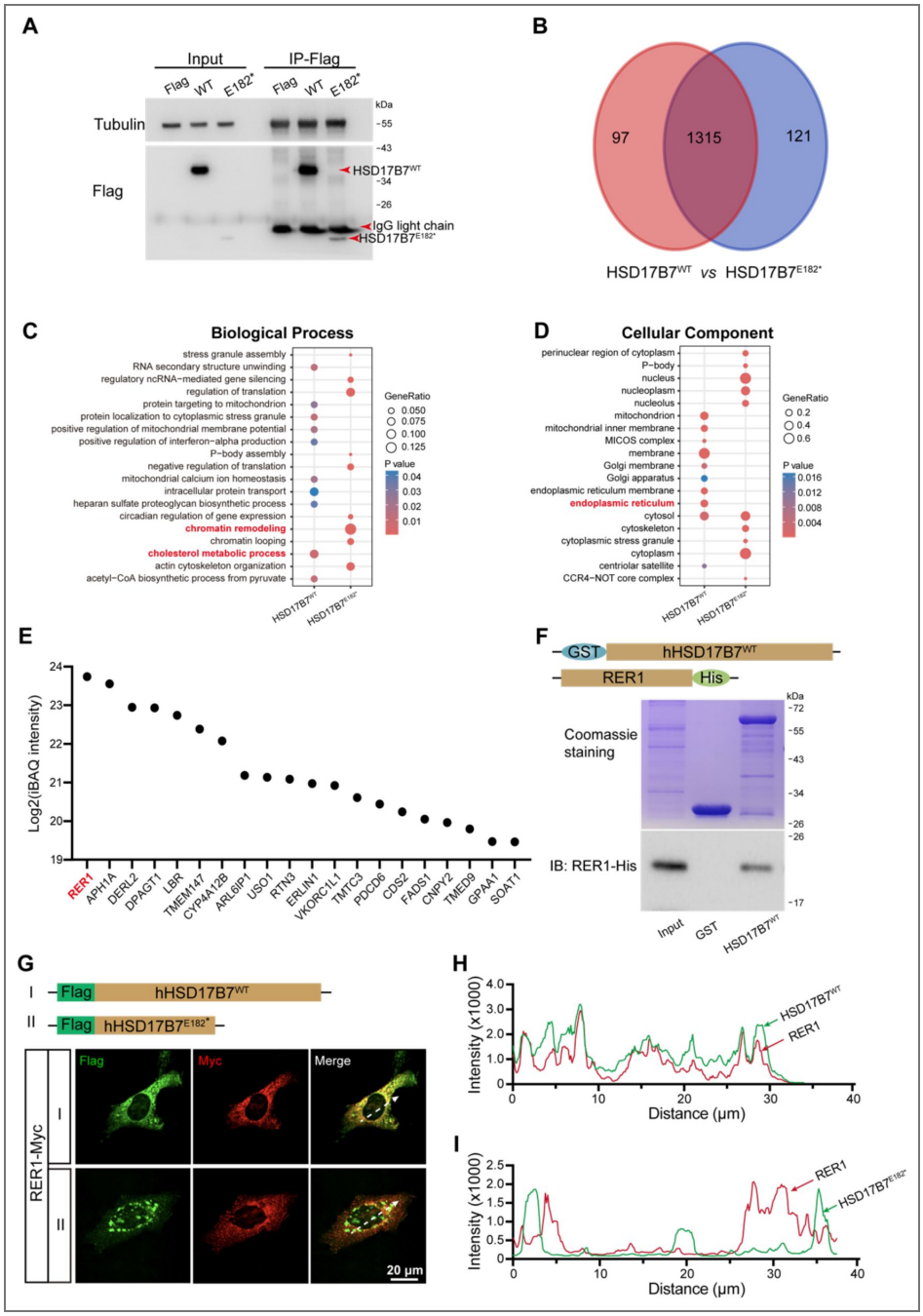

Figure 9. HSD17B7 interacts with RER1 to ensure ER localization.

(A) Co-immunoprecipitation of Flag-tagged HSD17B7 and HSD17B7^{E182*} from HEI-OC1 cells transfected with pCMV-Flag, pCMV-Flag-HSD17B7, or pCMV-Flag-HSD17B7^{E182*}. Cell lysates were immunoprecipitated using anti-Flag beads. Tubulin and IgG light chains served as loading and immunoprecipitation controls, respectively. (B) Venn diagram showing the overlap and uniqueness of interacting proteins identified for HSD17B7 (red) and HSD17B7^{E182*} (blue) by LC–MS/MS analysis. (C) Gene Ontology (GO) Biological Process enrichment analysis of proteins specifically associated with HSD17B7 or HSD17B7^{E182*}. (D) GO Cellular Component enrichment analysis of HSD17B7- and HSD17B7^{E182*}-specific interacting proteins. (E) Top 20 ER-localized proteins (ranked by iBAQ intensity) specifically associated with HSD17B7. (F) *In vitro* GST pull-down assays demonstrating direct interaction between HSD17B7 and RER1. The upper panel shows Coomassie blue staining of purified GST and GST-HSD17B7 proteins; the lower panel shows immunoblot detection of RER1-His. (G) Immunofluorescence staining of RER1-Myc in HEI-OC1 cells co-transfected with Flag-HSD17B7 or Flag-HSD17B7^{E182*}. White arrows indicate positions used for fluorescence intensity profiling. Scale bars, 20 μm. (H, I) Fluorescence intensity profiles showing co-localization of RER1 with HSD17B7 (H) but not with HSD17B7^{E182*} (I).

sensory hearing loss. In addition to the animal models, we identified a previously undescribed heterozygous nonsense variant in HSD17B7 (c.544G>T, p.E182*) in a patient with sporadic deafness. Functional analyses revealed that the residual HSD17B7^{E182*} protein alters subcellular localization and disrupts normal intracellular cholesterol distribution. Moreover, the mutation reduces mRNA half-life, decreases mRNA abundance, and significantly lowers protein expression. Collectively, these results suggest that the heterozygous c.544G>T (p.E182*) variant contributes to auditory dysfunction through potential pathogenic mechanisms: haploinsufficiency caused by reduced HSD17B7 expression and functional impairment due to altered cholesterol distribution. These mechanistic insights highlight the critical role of cholesterol homeostasis in MET and auditory-related function.

HSD17B7 was first identified as a prolactin receptor-associated protein in rats [44] and was proposed to be involved in estradiol biosynthesis [45, 46]. Subsequent biochemical studies demonstrated that HSD17B7 participated in cholesterol synthesis by catalyzing the reduction of zymosterone to zymosterol [47–49]. Consistent with this role, both *in vivo* and *in vitro* studies have shown that loss of HSD17B7 reduces cholesterol levels, whereas its overexpression increases cholesterol abundance. Previous studies have shown that HSD17B7 is expressed in the liver, heart, brain, eye, and ear [25, 26, 50], and scRNA-seq datasets have suggested its expression in mouse vestibular HCs [27]. Although the role of the *HSD17B7* gene in ovarian and breast cancer has been extensively explored in the literature [51–55], the role of the *HSD17B7* gene in auditory function remains unclear. Our results fill this gap by demonstrating that HSD17B7 is enriched in HCs, as supported by whole-mount *in situ* hybridization, immunostaining, and scRNA-seq analyses from our study and others [28, 31–33]. Given that loss of *hsd17b7* causes abnormal auditory-related behaviors, these data establish HSD17B7 as a conserved and essential regulator of hair cell function.

Cholesterol is a fundamental component of biological membranes, contributing to both their structural integrity and functional properties [56, 57]. Previous studies have shown that either excessive or insufficient cholesterol levels, as well as abnormal cholesterol distribution, are detrimental to the auditory system [7, 10, 11, 36, 37, 58, 59]. However, previous studies have largely focused on systemic or membrane cholesterol alterations and have not addressed the contribution of hair cell–intrinsic cholesterol biosynthesis. Smith–Lemli–Opitz syndrome (SLOS), caused by mutations in DHCR7, exemplifies how impaired cholesterol synthesis can lead to multisystem defects, including sensorineural hearing loss, although auditory function in these patients has not been extensively investigated [60]. Our study revealed that HSD17B7, a cholesterol biosynthetic enzyme, is enriched in sensory hair cells and plays a crucial role in maintaining cholesterol levels required for auditory-related function. It should be noted that some localization and cholesterol distribution analyses were performed using C-terminal EGFP-tagged HSD17B7 constructs, which may influence protein behavior. However, the central conclusions of this study are supported by complementary loss-of-function models, rescue experiments using untagged mRNA, and independent cholesterol perturbation assays, reducing reliance on any single overexpression or fusion-based approach.

Here, we found that loss of Hsd17b7 or expression of the truncated HSD17B7^{E182*} variant reduced cholesterol abundance and disrupted its intracellular distribution, resulting in defective MET function and auditory-related impairment. In contrast, overexpression of wild-type HSD17B7 elevated cholesterol levels but did not impair auditory-related behavior, suggesting that hair cell function requires a minimum critical cholesterol threshold rather than being sensitive to moderate cholesterol excess. Freeze-fracture studies have shown that the stereociliary membrane is densely enriched in cholesterol [61], supporting the notion that cholesterol is a key determinant of hair bundle membrane properties. Cholesterol is known to stiffen biological membranes [62], a biophysical feature that may influence MET channel gating [63, 64]. Consistent with this idea, cryo-EM studies have revealed conserved protein– lipid interactions within the TMC1/TMC2-containing MET channel complex [65, 66]. Together with our findings, these observations support a model in

which HSD17B7 regulates MET function by maintaining appropriate cholesterol abundance within hair cells. How cholesterol perturbations caused by HSD17B7 deficiency or mutation mechanistically alter MET channel activity remains an important question for future studies.

Dominant non-syndromic hearing loss is a common form of hereditary deafness [67–74] [75–78], and *de novo* mutations are frequently observed in patients with a negative family history. In the present study, both parents of the proband exhibited normal hearing and declined genetic testing, suggesting that the HSD17B7 (c.544G>T, p.E182*) variant may represent a de novo dominant mutation. This interpretation is consistent with previous reports showing that homozygous deletion of Hsd17b7 in mice is embryonic lethal, whereas heterozygous phenotypes have not been systematically characterized [79]. Notably, the mutant mRNA failed to rescue auditory defects in hsd17b7 mutants, and overexpression of $HSD17B7^{E182*}$ in wild-type animals impaired startle response. Although additional clinical cases will be required to confirm pathogenicity, our functional analyses provide experimental support for a negative effect of the $HSD17B7^{E182*}$ variant. Together with the marked reduction in mRNA and protein stability, these findings suggest that the $HSD17B7^{E182*}$ variant primarily acts through loss of function, with the possibility that aberrant intracellular localization and misdistribution of cholesterol further exacerbate HC dysfunction.

In summary, our study identifies HSD17B7 as a critical regulator of cholesterol synthesis in sensory hair cells and as an essential factor in normal MET and sound-evoked sensory responses. Additionally, we identified a sporadic nonsense mutation in the *HSD17B7* gene in patients with deafness and provided a mechanistic explanation. These findings uncover a previously unrecognized link between cholesterol biosynthesis and HC MET function and provide a molecular framework for exploring cholesterol-targeted therapeutic strategies for hearing loss.

Materials and Methods

Mouse and zebrafish husbandry

C57BL/6J mice were purchased from the Laboratory Animal Center of Nantong University and maintained in a barrier facility under a 12h light/12h dark cycle at 25℃. The day of vaginal plug observation was embryonic day 0.5 (E0.5), and the day of birth was defined as postnatal day 0 (P0). Zebrafish (*Danio rerio*) were raised and maintained at 28.5°C. Wild- type AB strain and the transgenic line *Tg(Brn3c: mGFP)* were used in the study described in our previous study [80]. The transgenic line *Tg(myo6b: D4H-mCherry)* was generated in this work. The embryonic stage is defined as described in the literature [81]. Embryos were collected following natural spawns and cultured in E3 medium (5 mM NaCl, 0.17 mM KCl, 0.33 mM $CaCl_2$, and 0.33 mM $MgSO_4$, pH 7.2). After 20 hours post-fertilization (hpf), embryos were incubated in E3 medium containing 0.2 mM phenylthiourea (PTU) to prevent pigmentation for *in situ* hybridization and imaging. All animal experiments were performed under the guidelines of the Institutional Animal Care and Use Committee of Nantong University.

Cell culture

The mouse auditory cell line HEI-OC1 was obtained from Prof. Renjie Chai and authenticated by short tandem repeat (STR) profiling (Shanghai Biowing Applied Biotechnology Co., Ltd). The cell lines were routinely tested negative for mycoplasma using the MycoBlue Mycoplasma Detection Kit (Vazyme Biotech, #D101-01), and cell aliquots from early passages were used. HEI-OC1 cells were cultured in DMEM (Wisent, #319-005-CL) medium supplemented with 10% FBS (Sigma-Aldrich, #F8318) in an incubator with 10% CO_2 at 33℃.

HEK293T (sex unknown) cells were obtained from the Shanghai Institute of Biochemistry and Cell Biology (SIBC) and authenticated by short tandem repeat (STR) profiling (Shanghai Biowing Applied Biotechnology Co., Ltd). The cell lines were routinely tested negative for mycoplasma using the MycoBlue Mycoplasma Detection Kit (Vazyme Biotech, #D101-01), and cell aliquots from early passages were used. Cells were cultured in DMEM (Wisent, #319-005-CL) medium supplemented with 10% FBS (Sigma-Aldrich, #F8318) in an incubator with 5% CO_2 at 37℃.

Antibodies

Primary antibodies used in this study included: anti-MYO7A monoclonal antibody (1:150, Developmental Studies Hybridoma Bank, #138-1); anti-HSD17B7 polyclonal antibody (1:150-1:1000, proteintech, #14854-1-AP); anti-Parvalbumin monoclonal antibody (1:500, sigma, #sab4200545); anti-MYC tag polyclonal antibody (1:200, proteintech, #16286-1-AP); anti-His antibody (1:2500, proteintech, # 66005-1-Ig); anti-DYKDDDDK tag mouse monoclonal antibody (1:200-1:5000, proteintech, #66008-4-Ig); anti-calnexin polyclonal antiboy (1:100, proteintech, #10427-2-AP); tubulin monoclonal antibody (1:5000, proteintech, #66031-1-Ig); goat anti-rabbit IgG(H+L) HRP (1:5000, MULTI SCIENCES, #GAR007); goat anti-mouse IgG(H+L) HRP (1:5000, MULTI SCIENCES, #GAM007); FITC goat anti-mouse IgG (H+L) (1:200, ABclonal, #AS001); Cy3 goat anti-rabbit IgG (H+L) (1:200, ABclonal, #AS007); anti-Digoxigenin-AP Fab fragments (1:1000, Roche, #11093274910).

RNA Isolation, Reverse Transcription (RT), and Quantitative Real-time PCR (RT-qPCR)

Total RNAs were extracted using TRIzol reagent (Invitrogen, #15596026) and treated with DNase I (Vazyme, #EN401) to remove genomic DNA contamination. RNA concentration was measured using a NanoDrop ND-2000 (Thermo Fisher Scientific, USA), and integrity was verified by agarose gel electrophoresis.

The cDNA was synthesized by using HiScript III RT SuperMix (Vazyme, #R323-01) following the manufacturer's directions. Subsequently, quantitative PCR was performed using the ChamQ SYBR qPCR Master Mix (Vazyme, #Q341-02) with the specified primers (*HSD17B7* primer, F: 5'-GACAAGC TTGGATCCATGCGAA -3', R: 5'-ACCTGGACAA TGGTGACCTC -3'; *Gapdh* primer, F: 5'-CACAGTCAAGGC CGAGAATGGGAAG-3', R: 5'-GTGGTTCACACCCATCACAAACATG) with a final volume of 20 μL under the following condition: 15 min at 50°C, 5 min at 95°C, and then 40 cycles at 95°C for 15 s and 60°C for 30 s. Relative expression levels for the *hsd17b7* gene were calculated using the $2^{-\triangle\triangle CT}$ method, normalized to the *gapdh*. All reactions were repeated in triplicate for each sample. The results were analyzed using the GraphPad Prism software (version 9.4.0).

Whole-mount in situ hybridization

The whole-mount in situ hybridization (WISH) of zebrafish was performed according to the following standard procedures. A 403 bp cDNA fragment of the zebrafish *hsd17b7* gene or a 472 bp cDNA fragment of the zebrafish *tmc1* gene was amplified via PCR using designed primers (*hsd17b7*-F: 5'-GACGTCCTCCAGTAATGCCC-3', *hsd17b7*-R: 5'-CATCTTGCTTGGT CGGGTGT-3'; *tmc1*-F: 5'-TTGGGCAGTGATGTGCTGTA-3', *tmc1*-R: 5'-GATGCTGTTT CTGCGTTGCT-3') and was cloned into the pGEM-T-easy vector. After linearization of the pGEM-T-easy vector, inserting the *hsd17b7* or *tmc1* fragment, the DIG RNA Labeling Kit (SP6) (Roche, #11175025910) was used to prepare digoxigenin-labeled *hsd17b7* or *tmc1* antisense mRNA probes through transcription *in vitro*. Subsequently, embryos at different developmental stages were hybridized with an *hsd17b7* or *tmc1* mRNA probe overnight after a series of treatments, including fixation in 4% paraformaldehyde in PBS, digestion in proteinase K (Roche, #3115879001), and incubation with a pre-hybridized mix. Finally, the alkaline phosphatase (AP)-conjugated antibody against digoxigenin (Roche, #11093274910) and the AP-substrate NBT/BCIP solution (Roche, #11681451001) were used to detect the *hsd17b7* or *tmc1* expression. The WISH images of zebrafish were acquired using a stereomicroscope (Olympus, MVX10, Japan).

Plasmids construction

The HSD17B7 and RER1 full-length cDNAs were PCR amplified from the HEK293T cDNA and cloned into the pGEX-TEV and pET-23b vectors, respectively. $HSD17B7^{E182*}$ was generated by site-directed mutagenesis. For cell transfection, the cDNA of HSD17B7 and $HSD17B7^{E182*}$ were subcloned into the pCMV-Flag vector, respectively. The cDNA of RER1 and $HSD17B7^{E182*}$ were subcloned into the pcDNA3.1-Myc-His A vector, respectively. eGFP was subcloned into pCMV-Flag-HSD17B7 and pCMV-Flag-$HSD17B7^{E182*}$, respectively. pCS2-D4H-mCherry was obtained from G. Peng's lab. For

plasmid injection of zebrafish, the *myo6b* promoter was subcloned into the pDestTol2 vector, followed by D4H-mCherry subcloned into the pDestTol2 vector. The cDNAs encoding the human protein of HSD17B7-eGFP and HSD17B7^{E182*}-eGFP were inserted into the p-mTol2-myo6b vector, then linking P2A-D4H-mCherry by overlap extension. For mRNA injection of zebrafish, the cDNAs encoding the human protein of HSD17B7 and HSD17B7^{E182*} were inserted into the pCS2^{+}, and likewise, the cDNAs encoding the zebrafish full-length protein of Hsd17b7 were inserted into the pCS2^{+}, which were linearized using NotI and then transcribed *in vitro* to generate mRNA. All constructs were verified by DNA sequencing.

Cell transfection

HEI-OC1 cells were transfected with plasmids using an X-treme GENE HP DNA transfection reagent (Roche, #6366236001) according to the manufacturer's protocol. After 36 hours or 48 hours of transfection, the cells were fixed or collected and subjected to further analyses, including western blots, Co-IP, IF, or RT-qPCR.

HEI-OC1 cells were transfected with small interfering RNA. The mouse *Hsd17b7* siRNA oligos (F: 5'-GGAGGUGUUUGAAACCAAUTT-3', R: 5'-AUUGGUUUCAAACACCUCCTT-3') were synthesized from GenePharma (Shanghai, China). Cells were transfected with siRNA oligos to knock down mHSD7B7 using Lipofectamine RNAiMAX (Invitrogen, #13778-150) according to the manufacturer's protocols. Approximately 1×10^{5} cells per well were placed in six-well plates. When the cell density reached 70-80%, 4 μL of control siRNA or mHsd17b7 siRNA was added to 150 μL of opti-MEM (Gibco, #31985070), then 5 μL Lipofectamine RANiMAX was added, incubated at room temperature for 5 min, and then added to the cell culture medium. After 48 hours of transfection, the transfected cells were harvested for Western blots or cholesterol assay.

mRNA stability assay

HEI-OC1 cells were transfected with plasmids using an X-treme GENE HP DNA transfection reagent. After 24 hours, the cells were treated with 10 μM actinomycin D (MCE, #HY-17559) for 0, 2, 4, 6, and 8 hours. Then, the collected cells and isolated RNA were used for RT-qPCR [82].

Immunostaining and image acquisition

Cultured cells grown on coverslips, after 36 hours of transfection, were fixed with 4% paraformaldehyde in PBS for 30 min at room temperature and washed 3 times with PBS, then permeabilized in 0.3% PBST (0.3% Triton X-100 in PBS) for 20 min. After three times washes with PBS, the cells were blocked with 10% FBS in PBS, followed by incubation with anti-primary antibodies overnight at 4°C, and then incubated with fluorescent dye-labelled secondary antibodies for 2 hours at room temperature before mounting using the mounting solution with DAPI (1:500, SouthernBiotech, #011-20).

The dissected mouse cochleae were fixed in 4% paraformaldehyde in PBS for 1 hour at room temperature. After 3 times washes with 0.1% PBST, the cochleae were briefly blocked with a blocking medium (PBS containing 1% Triton X-100 and 10% heat-inactivated donkey serum, pH 7.2) for 1 hour at room temperature, followed by incubation with the anti-primary antibody overnight at 4°C. The samples were then washed in 0.1% PBST and incubated with fluorescent dye-labelled secondary antibodies for 2 hours at room temperature, before mounting in mounting solution containing DAPI (1:500, SouthernBiotech, #011-20).

The immunostaining images of stained HEI-OC1 cells and cochlea were acquired by a Nikon confocal microscope with NIS-Elements software. For zebrafish live imaging, the larvae were anesthetized with tricaine MS-222 (Sigma, #A5040) and mounted in 0.6% low-melting agarose (Invitrogen, #16520050) with a lateral view. All reconstructed three-dimensional images and contrast adjustments were processed using Imaris X64 (version 9.0.1).

FM4-64 labeling

To investigate the basal activity of HCs, the FM4-64 (1:500, Invitrogen, #T13320) vital dye was used to specifically label functional HCs in the neuromasts. The staining procedures were carried out as described previously [29, 30, 83, 84]. The free-swimming larvae were incubated in 3 μM FM4-64 vital dye for 15 s at room temperature in the dark. Afterward, the fish were rinsed 3 times using a PTU medium and imaged. The images of stained hair cells were acquired by a Nikon confocal microscope with NIS-Elements software.

Measurement of total cholesterol

HEI-OC1 cells were homogenized in chloroform/methanol (2:1) to extract lipids and then centrifuged at 20,000 × *g* for 10 min. The organic phase was harvested and dried using nitrogen flow. Total cellular cholesterol was quantified using an Amplex Red cholesterol assay kit (Invitrogen, #A12216) through a multilabel reader (PerkinElmer, USA) according to the manufacturer's instructions.

Quantification of the relative fluorescence intensity of FM4-64 and D4H

Quantitative analysis of FM4-64 uptake in zebrafish lateral line hair cells and D4H-mCherry fluorescence in HEI-OC1 cells was performed at the single-cell level. For zebrafish experiments, hair cells were identified based on *Tg(Brn3c:mGFP)*. Individual hair cells within each neuromast were manually segmented using ImageJ, and the mean FM4-64 fluorescence intensity per hair cell was measured. Background fluorescence was determined from adjacent cell-free regions and subtracted from each measurement. For each larva, the average FM4-64 intensity was calculated by averaging values from all analyzed hair cells.

For D4H-mCherry cholesterol sensor analysis in HEI-OC1 cells, individual cells were segmented based on cell morphology, and the mean intracellular D4H-mCherry fluorescence intensity per cell was quantified. Background fluorescence was measured from cell-free regions within the same field of view and subtracted to normalize for imaging variability. Fluorescence intensities were then averaged across cells for each condition and used for statistical analysis. All fluorescence measurements were performed on raw images acquired under identical imaging settings across experimental groups.

Morpholino and mRNA injections

For inhibiting the expression of *hsd17b7*, *hsd17b7*-specific splicing-blocking morpholinos were designed and procured from Gene Tools, Inc., and the precise sequence was (5'-TGCAAACAGGTAAC AAAACTGTGTG-3'). The morpholino powder was dissolved in RNase-free water to prepare the working solution at a final concentration of 0.3 mM for subsequent operations. About 2 nL dose of morpholino work solution was microinjected into zebrafish embryos at the one-cell stage. To assess morpholino efficiency, embryos injected with morpholino were collected, and RNA was extracted and reverse-transcribed into cDNA. The designed primers flanking on exon 1 and exon 2 (F: 5'-TACACAGGCAAACGTTAGAAGC-3', R: 5'-CTTGAACTCCTCTGCACCCTT-3') were used to amplify the fragment containing the mis-splicing target site, which was located at the connection of exon 1 and intron 1. For rescue experiments, exogenous mRNA was first transcribed *in vitro*. Briefly, the designed primers (zebrafish *hsd17b7* mRNA primer, F: 5'-CGCGGATCCATGAAGAAAGTAGTTTTGGT-3', R: 5'-CCGGAATT CTCACATTCCATTTCTTTCTT-3'; human *HSD17B7* mRNA primer, F: 5'-CGGGATCC ATGCGAAAGGTGGTTTTGATC-3', R: 5'-GCTCTAGATTATAGGCATGA GCCACTGA-3'; human $HSD17B7^{E182*}$ mRNA primer, F: 5'-CGGGATCCATGCGAAAG GTGGTTTTGATC-3', R: 5'-GCTCTAGACTA GAGGCTGAAATTAGATT-3') were used to amplify target DNA containing the coding sequence. Subsequently, the pCS2 vector inserted into the amplified fragment was linearized as a template for mRNA transcription using the SP6 mMESSAGE mMACHINE Kit (Invitrogen, #AM1340). After purifying using the RNeasy Mini Kit (Qiagen, #74104), mRNA with a 70 ng/μL concentration was co-injected into one-cell stage embryos with morpholino for rescue experiments.

sgRNA/ Cas9 mRNA synthesis and injection

sgRNA was designed against the *hsd17b7* gene (ENSDARG00000088140) using the CRISPR design tool (*https://www.crisprscan.org*). The sgRNA specifically targeting exon 3 of *hsd17b7* (5'-GGGAA TCATGCCTAATCCCA-3') was first synthesized as follows. The GenCrispr sgRNA synthesis kit is used to generate a gRNA DNA template with a T7 promoter and to synthesize gRNA via *in vitro* transcription (Genscript Biotech Co., Ltd., Nanjing, China). The pXT7-zCas9 plasmid was linearized using XbaI and then transcribed *in vitro* to generate Cas9 mRNA using the mMESSAGE mMACHINE T7 kit (Invitrogen, #AM1344). At the one- cell stage, embryos were injected with a 2-3 μL solution containing 300 ng/μL Cas9 mRNA and 150 ng/μL sgRNA. The injected embryos were then grown in an E3 medium. At 24 hpf, genomic DNA was extracted from injected embryos, and potential CRISPR-induced mutations were identified by PCR. Primers used for identification were designed around the *hsd17b7* sgRNA target sites (F: 5'-AAAAACTTATTTTATTCCAGCCCAA-3', R: 5'-TTTCCAT GC AGCACTATCAAACAATT-3').

Startle Response Test

The acoustic startle reflex was performed as described previously [34, 85]. Briefly, A plastic plate attached to a mini vibrator was used to place 20 normal larvae at 5 days post-fertilization (dpf), while an infrared digital video tracking system was used to monitor their swimming behavior. 60 Hz tone bursts at two sound levels of 9 dB re. 1 $m{\cdot}s^{-2}$ were applied to the amplifier to drive the vibrator. Acoustic vibration stimuli lasting 30 ms, with an inter-stimulus interval of 180 s, were set and applied. Each sound vibration stimulus level was repeated 20 times, and the locomotion behavior of the larvae with C-shape motion in response to this stimulus was recorded. Finally, the movement's typical parameters of mean distance and peak velocity were analyzed to assess the startle response of larvae to sound vibration stimuli.

In vitro binding assay

GST and GST-HSD17B7 fusion proteins were immobilized on GSH resins and incubated with purified His-RER1 proteins overnight at 4℃ and extensively washed with washing buffer (0.3% PBST). Bound proteins were separated using SDS-PAGE and visualized with Coomassie Blue staining and Western blots.

Western blots

Frozen cells were lysed in RIPA buffer (50 mM Tris-HCl, 150 mM NaCl, 1 mM EDTA, 1% sodium deoxycholate, 1% w/v protein inhibitor (Roche, #4693132001)) for 30 min and centrifuged at 12,000 g for 15 min at 4℃. Protein concentrations were determined using a BCA protein assay kit (Thermo Fisher, #23227).

The proteins were separated on SDS-PAGE gels and subsequently transferred to a PVDF membrane (Millipore, USA). The membranes were blocked in blocking buffer (1 × TBS containing 0.5% milk and 0.5% Tween 20) for about 45 min at room temperature, then incubated overnight with primary antibodies in TBS containing 4% BSA, 1% Tween20, and 0.05% NaN_3. The next day, the PVDF membranes were incubated with the appropriate HRP-conjugated secondary goat antibodies for 2 hours at room temperature after extensive washing with a blocking buffer. The blots were detected using ECL TM Western Blotting Detection Reagents (GE, #RPN2106), and the acquired images were analyzed using ImageJ (version 1.8.0).

Co-IP, Mass spectrum, and Gene Ontology (GO) analysis

Cell lysates from pCMV-Flag, pCMV-Flag-HSD17B7, and pCMV-Flag-HSD17B7^{E182*} transfected cells were incubated with 30 μL of beads conjugated to anti-Flag antibodies (Smart-Lifesciences, #SA042001), respectively, overnight at 4℃. The next day, Flag beads were washed 3 times with lysis buffer, and the immune complexes were eluted with 2× SDS sample buffer and subjected to three samples for SDS-PAGE and mass spectrum analysis.

For mass spectrum, the immunoprecipitated HSD17B7 and HSD17B7^{E182*}-associated proteins were washed and dissolved in ammonium bicarbonate buffer (25 mM, pH 8.0), followed by trypsin digestion at 37℃ for 16 hours. The nano-LC-MS/MS experiments were performed with LTQ-Orbitrap MS (Thermo Fisher, USA) equipped with a Nano electrospray ion source.

For the Venn diagram and GO analysis, microarray analysis identified HSD17B7 and HSD17B7^{E182*}-specific associated proteins by mass spectrum (peptide ≥ 1, unique peptide ≥ 1, P value < 0.05). Cellular component GO term enrichment analysis was performed using the web-based DAVID software [86]. Ontology networks were further investigated and visualized using R (version 4.4.1).

Public scRNA-seq datasets and expression profiling of hsd17b7

Zebrafish scRNA-seq data were downloaded from NCBI Gene Expression Omnibus (GSE221471) [28]. The basic procedure for single-cell integrated data analysis was performed using Seurat 4.0.1 [87]. Cell clusters corresponding to LLHCs, MHCs, CHCs, supporting cells, and mantle cells were selected based on previously published annotations. Feature plots, violin plots, and average expression analyses were used to examine the expression pattern of *hsd17b7* across cell types. To assess dynamic changes in *hsd17b7* expression during HC differentiation, trajectory analysis was performed using Monocle 3 (v1.0.1). Cells were ordered along pseudotime, with mantle cells as the root population, and gene-expression changes were visualized along the inferred developmental trajectory.

Mouse scRNA-seq data were downloaded from previous articles (GSE71982, GSE168901, GSE202920) [31–33]. The basic procedure for single-cell integrated data analysis and batch-effect correction was performed using Seurat 4.0.1 [87]. We selected four cell populations for re-analysis, including inner hair cells, outer hair cells, utricle hair cells, and crista hair cells.

Single-cell RNA sequencing of control and hsd17b7 mutant hair cells

To investigate genotype-dependent transcriptional remodeling in sensory hair cells, we performed single-cell RNA sequencing on fluorescence-activated cell sorting (FACS)-isolated hair cells from control and *hsd17b7* mutant zebrafish.

Isolation of hair cells and single-cell RNA sequencing

mGFP-positive hair cells were isolated from control and *hsd17b7* mutant zebrafish larvae by fluorescence-activated cell sorting (FACS). Dissociated cells were gated to exclude debris and doublets, and viable mGFP^{+} cells were collected for downstream analysis. Single-cell RNA sequencing libraries were generated using the 10× Genomics Chromium platform according to the manufacturer's instructions. Libraries were sequenced on an Illumina platform to obtain paired-end reads. Raw sequencing data were processed using the Cell Ranger pipeline (10× Genomics) to generate gene expression matrices for each sample. Downstream analyses were performed in R using the Seurat package.

Data preprocessing, integration, and cell type annotation

Cells with low gene counts or high mitochondrial transcript proportions were excluded to remove low-quality cells. Gene expression matrices from control and *hsd17b7* mutant samples were normalized and integrated using Harmony to correct for batch effects while preserving biological variation.

Dimensionality reduction was performed using principal component analysis (PCA), followed by Uniform Manifold Approximation and Projection (UMAP) for visualization. Clustering was conducted using a shared nearest neighbor (SNN) graph-based approach. Cell clusters were annotated based on established marker genes for hair cells and supporting cells. Hair cells were identified by robust expression of *myo6b*, while inner ear and lateral line hair cell subtypes were distinguished by *lhfpl5a* and *lhfpl5b*, respectively. Supporting cell populations were annotated

using *stm* as a pan–supporting cell marker, with *otogl* and *irg1l* marking inner ear and lateral line supporting cells, respectively. Cell type annotations were validated using both violin plots and Nebulosa density visualizations

Pseudobulk differential expression analysis

To assess genotype-dependent transcriptional changes while accounting for cell-to-cell variability, pseudobulk differential expression analysis was performed for hair cells. Gene expression counts from individual cells were aggregated by genotype to generate pseudobulk profiles. Differential expression between control and *hsd17b7* mutant HCs was assessed using a generalized linear model framework. Genes with an adjusted p-value < 0.05 were considered differentially expressed. Results were visualized using volcano plots, with upregulated and downregulated genes highlighted accordingly.

Gene Ontology and pathway enrichment analysis

Differentially expressed genes were subjected to Gene Ontology (GO) biological process enrichment analysis using curated annotation databases [88]. Enrichment analyses were performed separately for upregulated and downregulated gene sets. Significantly enriched GO terms were visualized, and representative genes contributing to each term were illustrated using Sankey diagrams to highlight functional relationships between gene sets and biological processes.

Gene set enrichment analysis (GSEA) was additionally performed to assess coordinated changes in cholesterol biosynthesis–associated pathways at the transcriptome-wide level. Ranked gene lists derived from pseudobulk differential expression results were used as input, and enrichment significance was assessed using normalized enrichment scores and adjusted p-values.

Module score analysis of MET- and cholesterol-related gene sets

Module scores were computed using the AddModuleScore function in Seurat, based on normalized expression values from the RNA assay. Module score distributions were examined separately in lateral line hair cells (LL_HCs) and inner ear hair cells (IE_HCs). Differences between control and *hsd17b7* mutant samples were assessed using the Wilcoxon rank-sum test. Results were visualized using heatmaps, violin plots, and ridge plots. Ridge plots were generated using z-scored module scores to illustrate population-wide shifts in transcriptional states rather than the emergence of discrete subpopulations.

Visualization and statistical analysis

UMAP feature plots, heatmaps, violin plots, and ridge plots were generated using Seurat and associated R visualization packages. Nebulosa density plots were used to visualize spatial expression patterns of marker genes across low-dimensional embeddings. Statistical analyses were performed using R, and exact p values or significance levels are reported in the corresponding figure panels and legends.

Whole-exome sequencing and Sanger sequencing analyses

Whole-exome sequencing was performed in the proband Ⅱ 1. Genomic DNA samples were extracted from whole blood samples of the proband Ⅱ 1 (Figure 5A).

The exomes and flanking intronic regions from whole blood DNA samples were captured by Agilent SureSelect Human All Exon Kit (Agilent Technologies, USA). The captured DNA was sequenced on the Illumina HiSeq 4000 sequencing platform (Illumina, USA). Bioinformatics were aligned to the NCBI build37/hg19 assembly using the BWA (version 0.7.12) software. Each sample was covered to an average sequencing depth of at least 100×. SNPs and indels were identified using the GATK HaplotypeCaller software. Candidate pathogenic variants were defined as nonsense, missense, splice-site, and indel variants with allele frequencies of 0.001 or less in public variant databases (dbSNP, 1000 Genomes, ESP6500, nci60, GnomAD) and in disease databases (COSMIC, ClinVar, OMIM, GWAS). Genotypes distributed every 0.3 cM of genomic region were

chosen for calculation of the logarithm of odds (LOD) scores using the Merlin v. 1.1.2 parametric linkage analysis package. The proband Ⅱ 1 was genotyped by Sanger sequencing analyses with designed primers (F: 5'-GTACTCTGATTGGTGACGGGTGAG-3', R: 5'-GACAGTCATAGTTCATAGTTTATT-3')

Quantification and statistical analysis

GraphPad Prism 9 (version 9.4.0) supported the whole statistical analysis. All data presented as mean ± SD or mean ± SEM. An unpaired two-tailed Student's t-test was performed for two-group comparisons, while multiple comparisons were illustrated using one-way ANOVA. The p-value less than 0.05 ($p \leq 0.05$) was considered significantly different. $p \leq 0.05$, $p \leq 0.01$, $p \leq 0.001$, and $p \leq 0.0001$ were symbolized with "*, **, ***, and ****", respectively, and "ns" represented no significance, $p > 0.05$.

Data availability

The plasmids and zebrafish lines generated in this study are available on request to the Lead Contact. The published article includes all datasets generated or analyzed during this study. Any additional information required to reanalyze the data reported in this paper is available from the Lead Contact upon request. Sequencing data have been deposited in GEO under accession codes GSE319132.

Supplementary Figures

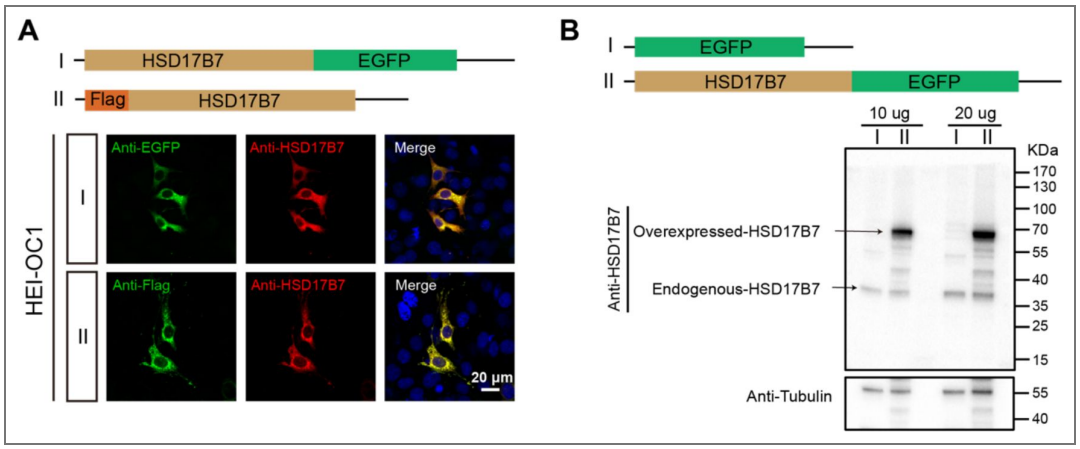

Figure S1. Validation of HSD17B7 antibody specificity in HEI-OC1 cells. (A) HEI-OC1 cells were transfected with pCMV-Flag-HSD17B7 or pCMV-HSD17B7-EGFP constructs. Immunofluorescence staining using an anti-HSD17B7 antibody showed strong co-localization with both FLAG and EGFP signals, confirming the specificity of the antibody for HSD17B7. (B) Western blot analysis of cells transfected with the constructs further verified the specific detection of HSD17B7 protein by the anti-HSD17B7 antibody.

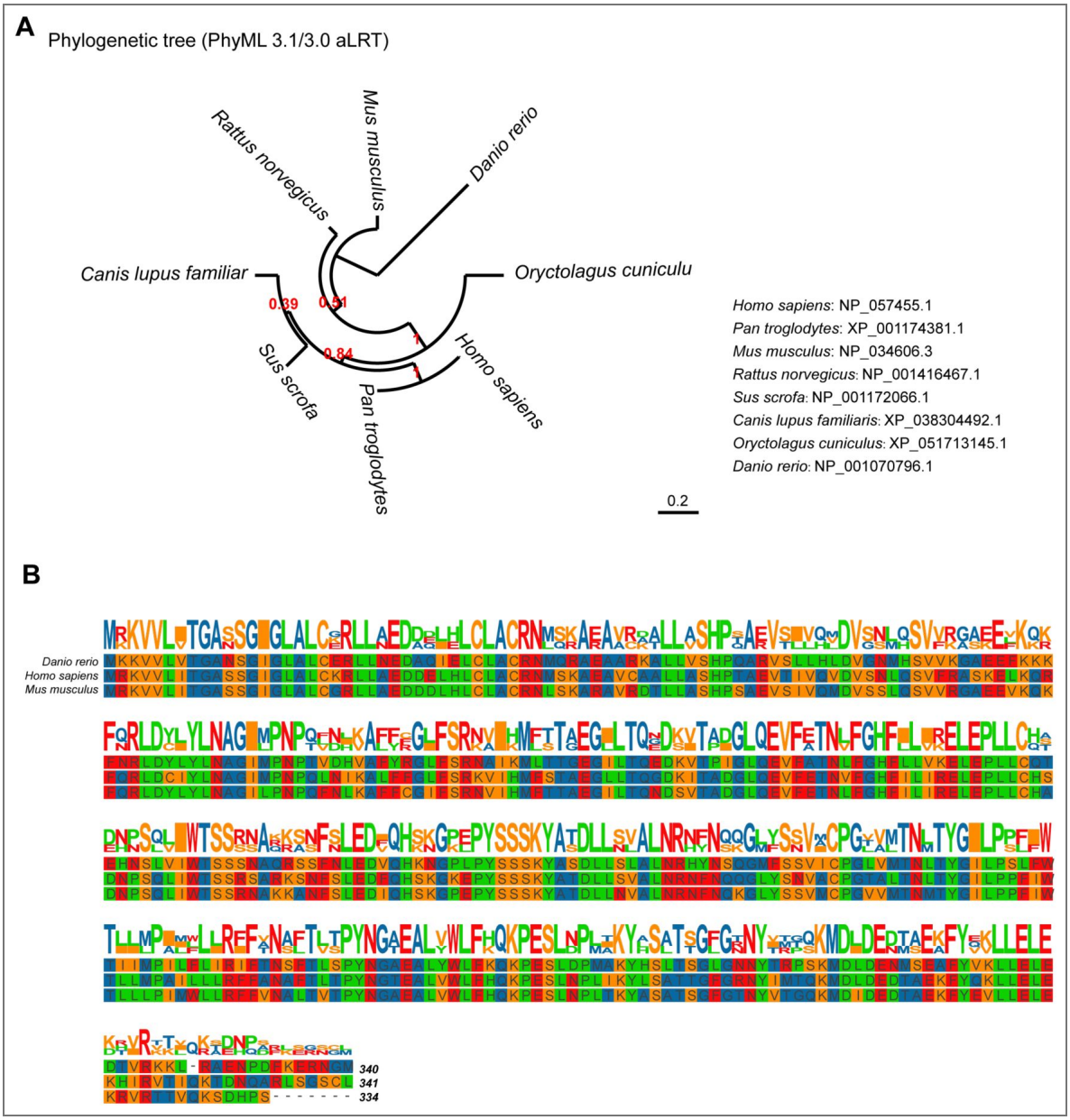

Figure S2. Evolutionary conservation of Hsd17b7.

(A) Evolutionary conservation of Hsd17b7. The phylogenetic tree was reconstructed using Phylogeny. fr (v3.1/3.0, aLRT) by maximum likelihood, and its graphical representation and editing were performed with TreeDyn (v198.3). (B) The amino acid sequence was analyzed using TBtools multiple-sequence alignment of Hsd17b7 orthologs.

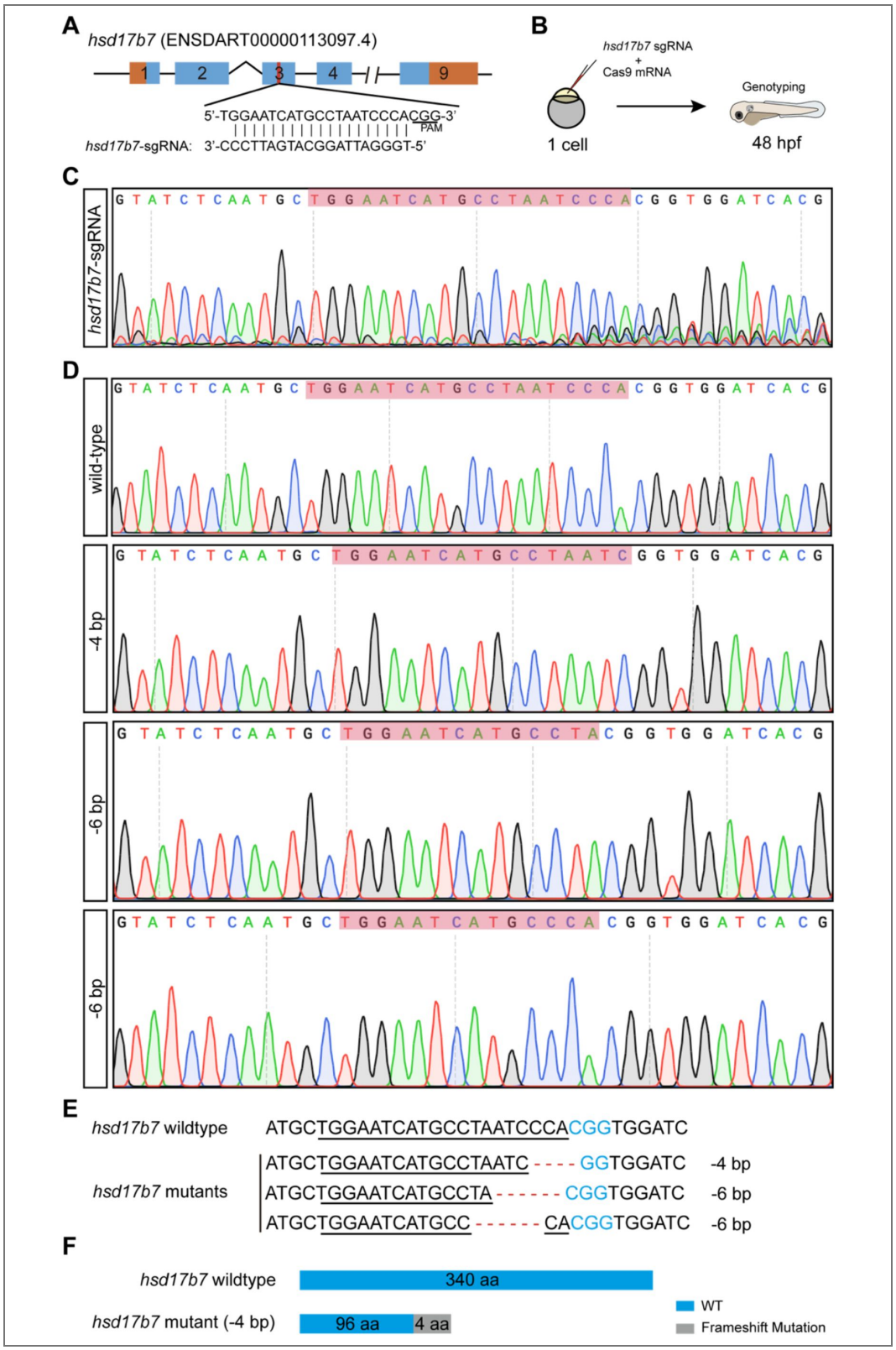

Figure S3. Generation of *hsd17b7* mutant using the CRISPR/Cas9 system in zebrafish.

(A) Schematic diagram showing sgRNA and the target site on the exon 3 of the *hsd17b7* gene. (B) Schematic diagram showing the *hsd17b7* mutant establishment process. (C) Mutation pattern of sgRNA and Cas9-injecting embryos. (D) Sequencing Chromatograms of -4 bp, -6 bp, and -6 bp deletion mutant line. (E) Three types of mutations were identified by sequencing and screening. (F) Schematic diagram of the predicted proteins encoded by the -4 bp deletion mutant line.

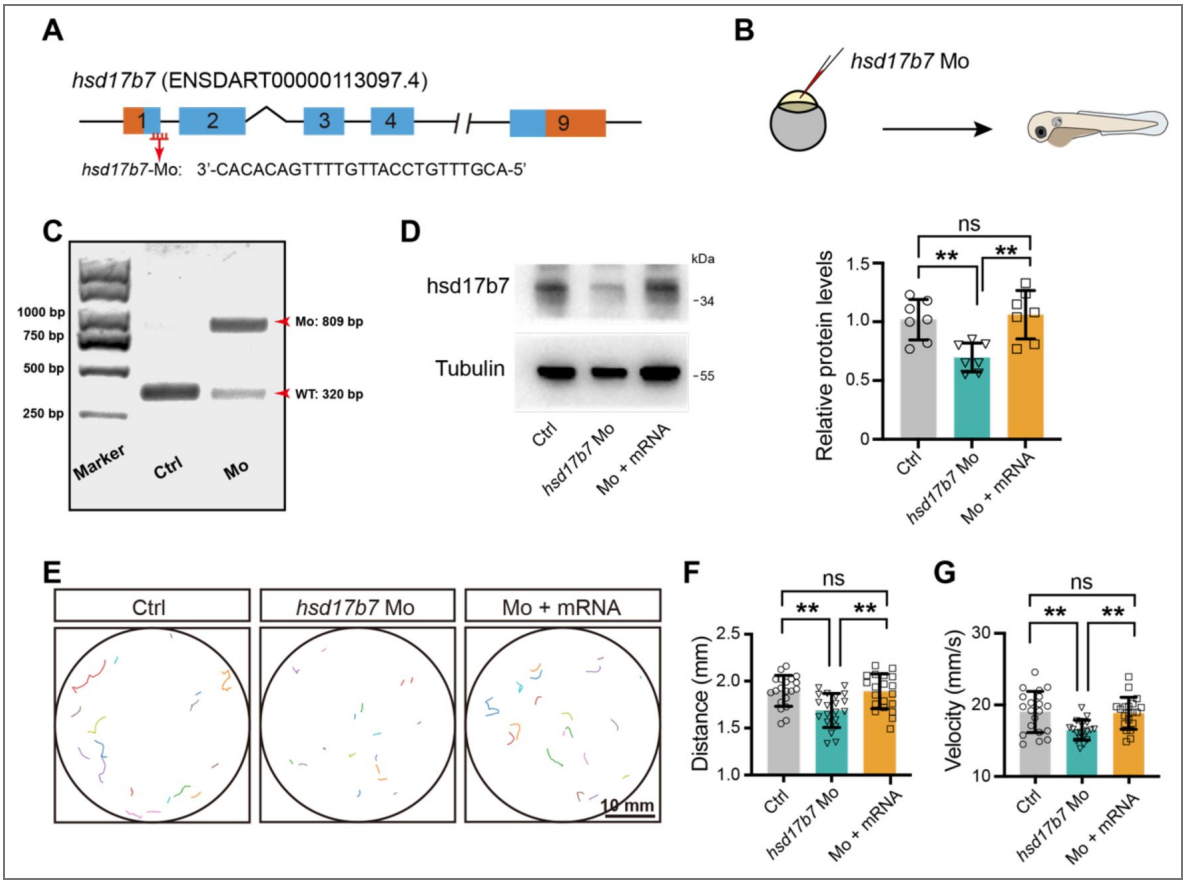

Figure S4. Knockdown of *hsd17b7* impairs auditory-evoked startle responses in zebrafish.

(A) Schematic illustration of morpholino targeting the exon1/intron1 splice junction of the *hsd17b7* gene. (B) Schematic diagram of one-cell embryo injection of *hsd17b7* morpholino (Mo) into wild-type embryos. (C) The efficiency of morpholino was detected by RT-PCR. (D) Western blots showing hsd17b7 protein levels of control, *hsd17b7* morphants, and *hsd17b7* mRNA-rescued groups at 3 dpf. Quantification of relative hsd17b7 protein is shown on the right (n=7). One-way ANOVA followed by Tukey's multiple comparisons, $^{**}P < 0.01$, ns, non-significant ($p > 0.05$), mean ± SD. (E) Representative locomotion trajectories of larvae exhibiting behavior responses to a single acoustic stimulus (9 dB re. 1 $m{\cdot}s^{-2}$, 60 Hz tone burst) in control, *hsd17b7* morphants, and *hsd17b7* mRNA rescued groups, respectively. Scale bars, 10 mm. (F, G) Quantification of the mean distance and peak velocity of movement of 5 dpf larvae in response to acoustic stimulation shown in (E) (n=20). One-way ANOVA followed by Tukey's multiple comparisons, $^{**}P < 0.01$, ns, non-significant ($p > 0.05$), mean ± SEM.

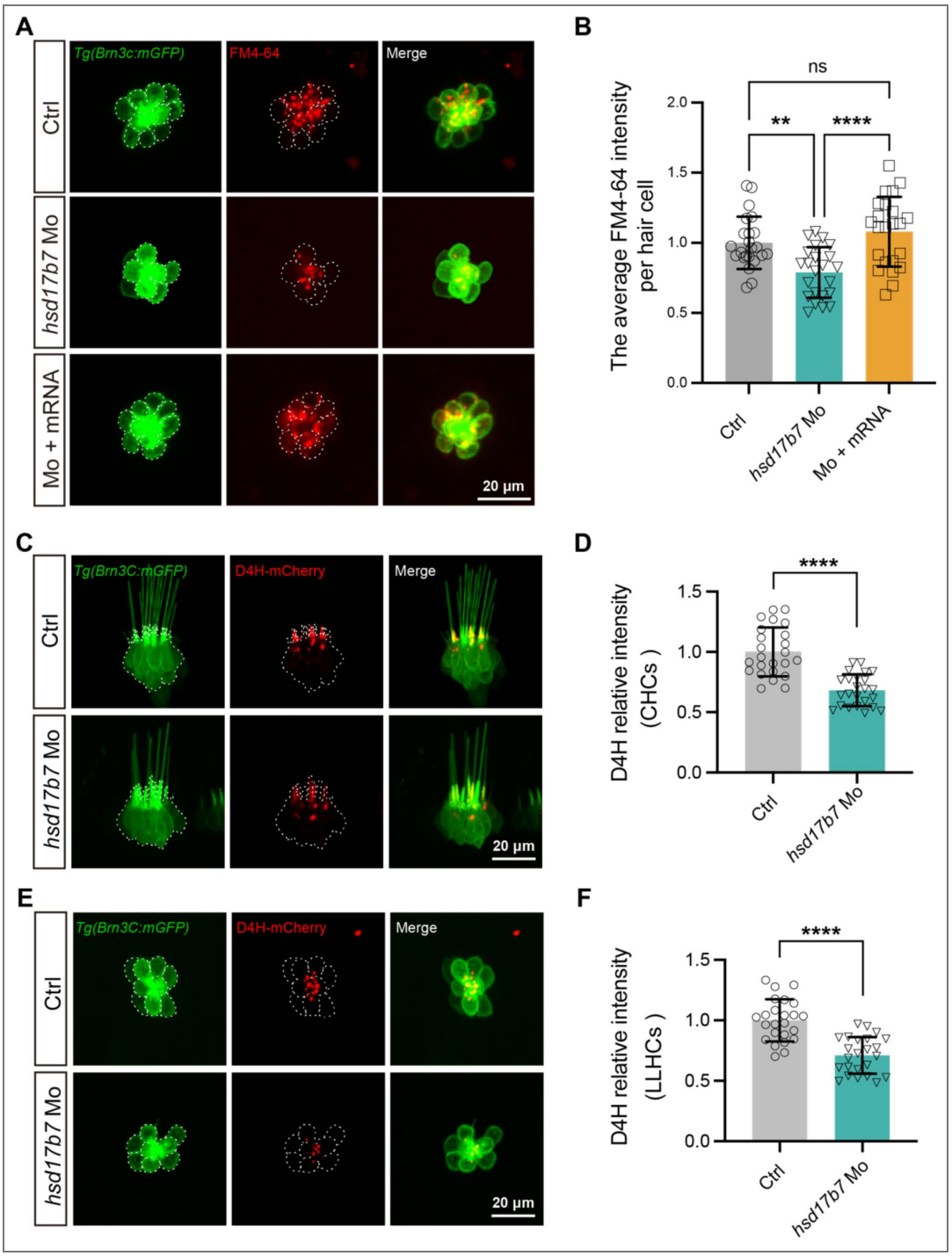

Figure S5. Knockdown of *hsd17b7* leads to MET dysfunction and decreases cholesterol levels in zebrafish.

(A) Representative images of lateral line hair cells (LLHCs, green) and FM4-64–labeled functional HCs (red) at 5 dpf *Tg(Brn3c:mGFP)* larvae from control, *hsd17b7* morphants, and *hsd17b7* mRNA rescued groups, respectively. White dashed indicates LLHCs. Scale bars, 20 μm. (B) Quantification of the FM4-64 relative intensity per HC for (A) (n=23). *P* values were determined using a one-way ANOVA test followed by Tukey's multiple comparisons. ****$P < 0.0001$; **$P < 0.01$;ns, non-significant ($p > 0.05$). (C) Representative images of the cholesterol probe D4H–mCherry (red) in crista hair cells (CHCs, green) from control and *hsd17b7* morphants at 4 dpf. White dashed outlines indicate CHCs. Scale bars, 20 μm. (D) Quantification of relative D4H fluorescence intensity in CHCs shown in (C) (n = 24). Unpaired two-tailed Student's *t* test, ****$P < 0.0001$, mean ± SD. (E) Representative images of D4H–mCherry (red) in LLHCs (green) from control and *hsd17b7* morphants at 4 dpf. White dashed outlines indicate LLHCs. Scale bars, 20 μm. (F) Quantification of relative D4H fluorescence intensity in LLHCs shown in (E) (n = 24). Unpaired two-tailed Student's *t* test, ****$P < 0.0001$, mean ± SD.

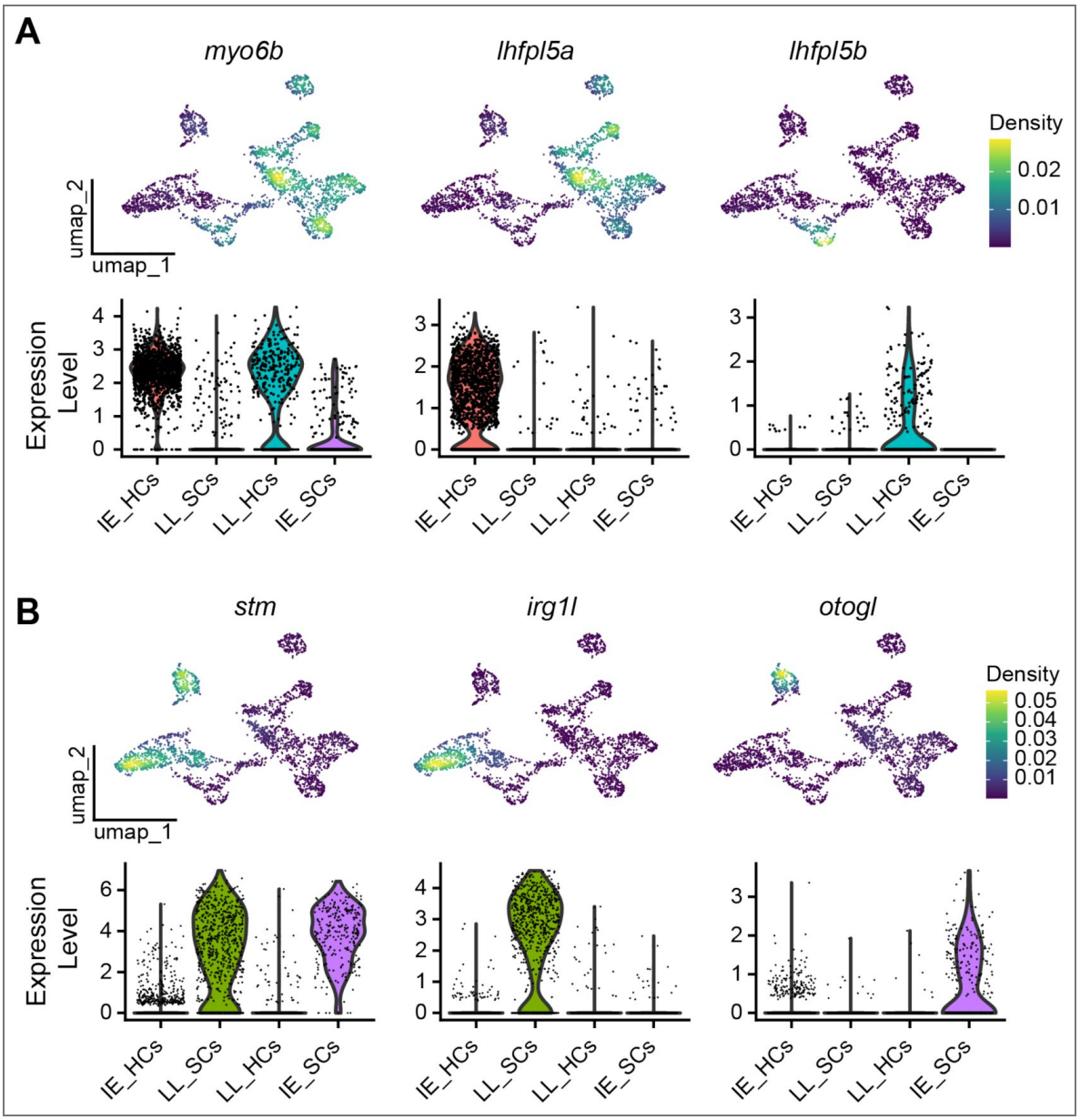

Figure S6. Validation of cell type annotation and cholesterol- and MET-related transcriptional states in hair cells.

(A) Nebulosa density plots and violin plots showing the expression of canonical hair cell markers across the integrated scRNA-seq dataset. The pan–hair cell marker *myo6b* is broadly enriched in hair cell populations, while *lhfpl5a* and *lhfpl5b* specifically mark inner ear hair cells (IE_HCs) and lateral line hair cells (LL_HCs), respectively, confirming accurate hair cell annotation. (B) Nebulosa density plots and violin plots of supporting cell marker genes. The general supporting cell marker *stm*, together with *otogl* (IE_SCs) and *irg1l* (LL_SCs), show cell type–restricted expression patterns, validating the identification of supporting cell populations in both inner ear and lateral line systems.

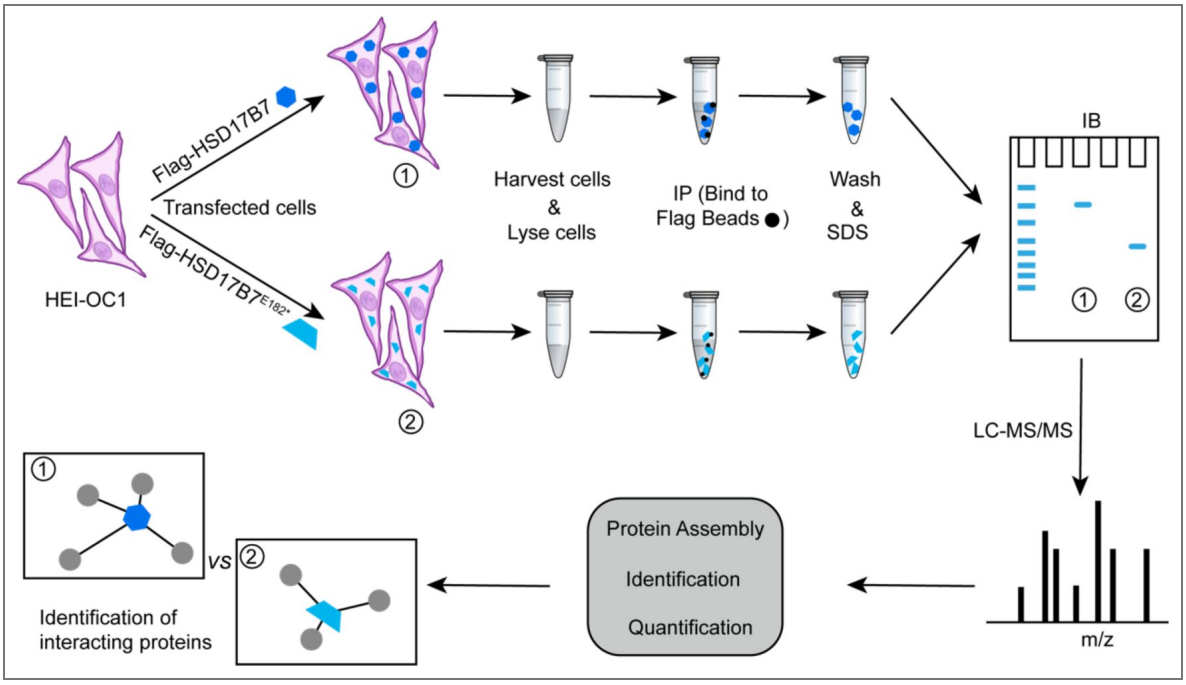

Figure S7. **Schematic of the experimental process for immunoprecipitation and LC-MS/MS to identify HSD17B7 and HSD17B7^{E182*} interacted proteins.**

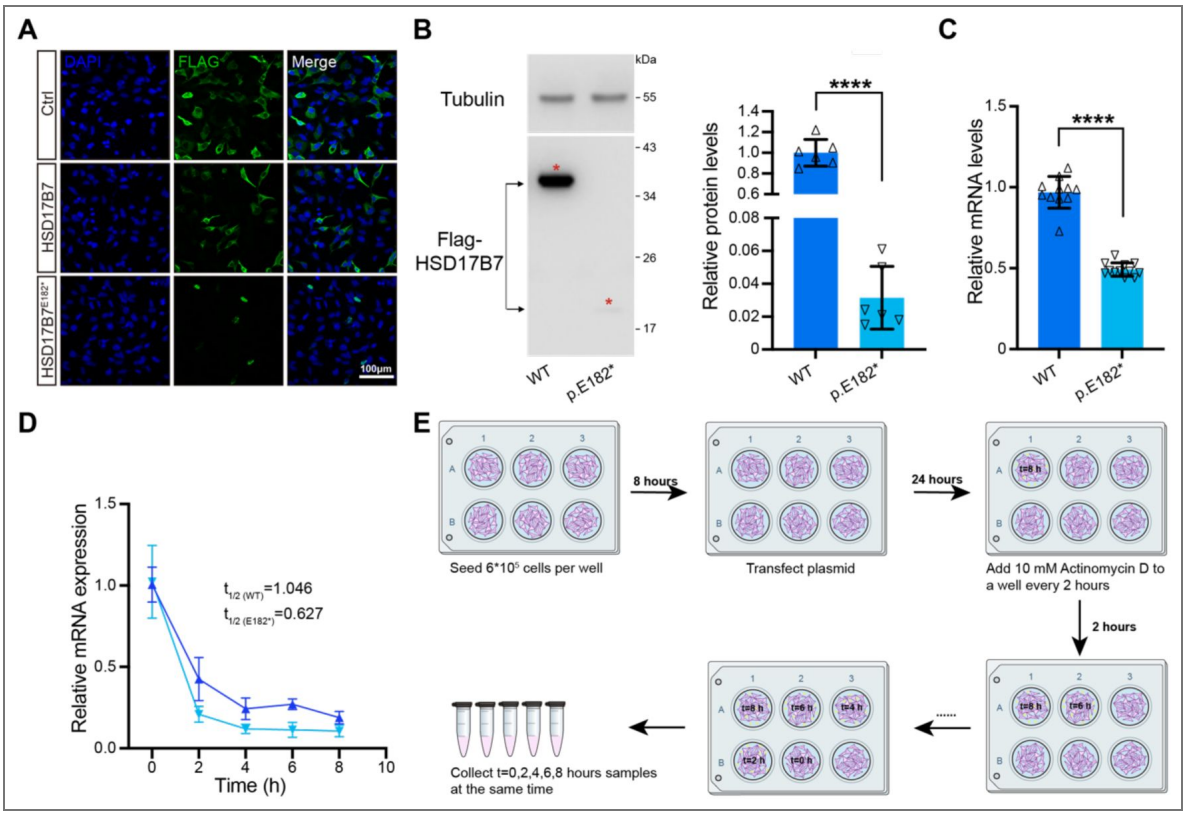

Figure S8. E182* mutation decreased HSD17B7 protein levels, mRNA levels, and the half-life periods.

(A) Representative images of HEI-OC1 cells transfected with pCMV-Flag, pCMV-Flag-HSD17B7, or pCMV-Flag-HSD17B7E182* plasmids. (B) Western blots showing the protein levels of exogenously expressed HSD17B7 in HEI-OC1 cells transfected with pCMV-Flag-HSD17B7 (WT) and pCMV-Flag-HSD17B7^{E182*} (p.E182*) plasmids, respectively. Tubulin was used as the loading control. Red stars indicated HSD17B7 and HSD17B7^{E182*}. Quantification of relative protein levels was shown on the right (n=6). Unpaired two-tailed Student's *t* test, ****$P < 0.0001$, mean ± SD. (C) RT-qPCR showing the mRNA level of *HSD17B7* and *HSD17B7*^{E182*} in transfected HEI-OC1 cells (n=11). Unpaired two-tailed Student's *t* test, ****$P < 0.0001$, mean ± SD. (D) RT-qPCR analysis of mRNA stability in transfected HEI-OC1 cells (n=12). (E) Schematic diagram illustrating the experimental workflow for mRNA stability analysis and sample collection.

Acknowledgements

This work was supported by the National Natural Science Foundation of China Grants (32200783 to Y.Q.S; 92368104 and 32350017 to D.L.) and the Natural Science Foundation of Jiangsu Province Grants (BK20220607 to Y.Q.S).

Additional information

Author Contributions

Conceptualization, Y.Q.S., Z.Y.W., and D.L.; methodology, Y.Q.S., Z.Y.W., M.J.Z., Xu.W., F.P.Q.; investigation, Y.Q.S., Z.Y.W., and D.L.; writing - original draft, Y.Q.S., Z.Y.W., Xi.W., and D.L.; writing - review & editing, Y.Q.S., Z.Y.W., and D.L.; funding acquisition, Y.Q.S., and D.L.; resources, Z.M.J., and J.C.; supervision, D.L and J.C.

Funding

Funder	Grant reference number	Author
National Natural Science Foundation of China	32200783	Yuqian Shen
National Natural Science Foundation of China	92368104	Dong Liu
National Natural Science Foundation of China	32350017	Dong Liu
Natural Science Foundation of Jiangsu Province Grants	BK20220607	Yuqian Shen

Author ORCID iDs

Ziyang Wang: https://orcid.org/0009-0003-9470-8914
Fuping Qian: https://orcid.org/0000-0001-5745-9304
Dong Liu: https://orcid.org/0000-0002-2764-6544

References

1. **Hu X.Y.**, et al. (2016) [Prevalence of hearing disorders in China: a population-based survey in four provinces of China]. *Zhonghua Er Bi Yan Hou Tou Jing Wai Ke Za Zhi* **51**:819-825 https://doi.org/10.3760/cma.j.issn.1673-0860.2016.11.004 | PubMed
2. **Ingham N.J.**, et al. (2019) Mouse screen reveals multiple new genes underlying mouse and human hearing loss. *PLoS Biol* **17**:e3000194 https://doi.org/10.1371/journal.pbio.3000194 | PubMed
3. **Pfrieger F.W.**, Ungerer N. (2011) Cholesterol metabolism in neurons and astrocytes. *Prog Lipid Res* **50**:357-71 https://doi.org/10.1016/j.plipres.2011.06.002 | PubMed
4. **Yoon J.H.**, et al. (2022) Brain lipidomics: From functional landscape to clinical significance. *Sci Adv* **8**:eadc9317 https://doi.org/10.1126/sciadv.adc9317 | PubMed
5. **Dietschy J.M.**, Turley S.D. (2001) Cholesterol metabolism in the brain. *Curr Opin Lipidol* **12**:105-12 https://doi.org/10.1097/00041433-200104000-00003 | PubMed
6. **Wu J.**, et al. (2023) Impact of cholesterol homeostasis within cochlear cells on auditory development and hearing loss. *Front Cell Neurosci* **17**:1308028 https://doi.org/10.3389/fncel.2023.1308028 | PubMed
7. **Ding D.**, et al. (2020) Hydroxypropyl-β-cyclodextrin causes massive damage to the developing auditory and vestibular system. *Hear Res* **396**:108073 https://doi.org/10.1016/j.heares.2020.108073 | PubMed
8. **Levic S.**, Yamoah E.N. (2011) Plasticity in membrane cholesterol contributes toward electrical maturation of hearing. *J Biol Chem* **286**:5768-73 https://doi.org/10.1074/jbc.m110.186486 | PubMed

9. **Wang H.,** et al. (2019) Deletion of OSBPL2 in auditory cells increases cholesterol biosynthesis and drives reactive oxygen species production by inhibiting AMPK activity. *Cell Death Dis* **10**:627 https://doi.org/10.1038/s41419-019-1858-9 | PubMed
10. **Yao J.,** et al. (2019) OSBPL2-disrupted pigs recapitulate dual features of human hearing loss and hypercholesterolaemia. *J Genet Genomics* **46**:379-387 https://doi.org/10.1016/j.jgg.2019.06.006 | PubMed
11. **Xing G.,** et al. (2015) Identification of OSBPL2 as a novel candidate gene for progressive nonsyndromic hearing loss by whole-exome sequencing. *Genet Med* **17**:210-8 https://doi.org/10.1038/gim.2014.90 | PubMed
12. **Maas R.R.,** et al. (2017) Progressive deafness-dystonia due to SERAC1 mutations: A study of 67 cases. *Ann Neurol* **82**:1004-1015 https://doi.org/10.1002/ana.25110 | PubMed
13. **King K.A.,** et al. (2014) Hearing loss is an early consequence of Npc1 gene deletion in the mouse model of Niemann-Pick disease, type C. *J Assoc Res Otolaryngol* **15**:529-41 https://doi.org/10.1007/s10162-014-0459-7 | PubMed
14. **Wang Q.,** et al. (2020) Systematic Transcriptome Analysis of Noise-Induced Hearing Loss Pathogenesis Suggests Inflammatory Activities and Multiple Susceptible Molecules and Pathways. *Front Genet* **11**:968 https://doi.org/10.3389/fgene.2020.00968 | PubMed
15. **Sai N.,** et al. (2020) Involvement of Cholesterol Metabolic Pathways in Recovery from Noise-Induced Hearing Loss. *Neural Plast* **2020**:6235948 https://doi.org/10.1155/2020/6235948 | PubMed
16. **Milon B.,** et al. (2021) A cell-type-specific atlas of the inner ear transcriptional response to acoustic trauma. *Cell Rep* **36**:109758 https://doi.org/10.1016/j.celrep.2021.109758 | PubMed
17. **Zhou Y.,** et al. (2018) The susceptibility of cochlear outer hair cells to cyclodextrin is not related to their electromotile activity. *Acta Neuropathol Commun* **6**:98 https://doi.org/10.1186/s40478-018-0599-9 | PubMed
18. **Ory D.S.,** et al. (2017) Intrathecal 2-hydroxypropyl-β-cyclodextrin decreases neurological disease progression in Niemann-Pick disease, type C1: a non-randomised, open-label, phase 1-2 trial. *Lancet* **390**:1758-1768 https://doi.org/10.1016/s0140-6736(17)31465-4 | PubMed
19. **Tang T.H.,** et al. (2019) Can Nutritional Intervention for Obesity and Comorbidities Slow Down Age-Related Hearing Impairment?. *Nutrients* **11** https://doi.org/10.3390/nu11071668 | PubMed
20. **Honkura Y.,** et al. (2019) Effects of enriched endogenous omega-3 fatty acids on age-related hearing loss in mice. *BMC Res Notes* **12**:768 https://doi.org/10.1186/s13104-019-4809-8 | PubMed
21. **Sodero A.O.,** et al. (2023) Phytosterols reverse antiretroviral-induced hearing loss, with potential implications for cochlear aging. *PLoS Biol* **21**:e3002257 https://doi.org/10.1371/journal.pbio.3002257 | PubMed
22. **Saloniemi T.,** et al. (2012) The diversity of sex steroid action: novel functions of hydroxysteroid (17β) dehydrogenases as revealed by genetically modified mouse models. *J Endocrinol* **212**:27-40 https://doi.org/10.1530/joe-11-0315 | PubMed
23. **Shehu A.,** et al. (2011) The stimulation of HSD17B7 expression by estradiol provides a powerful feed-forward mechanism for estradiol biosynthesis in breast cancer cells. *Mol Endocrinol* **25**:754-66 https://doi.org/10.1210/me.2010-0261 | PubMed
24. **Hilborn E.,** Stål O., Jansson A. (2017) *Estrogen and androgen-converting enzymes 17β-hydroxysteroid dehydrogenase and their involvement in cancer: with a special focus on 17β-hydroxysteroid dehydrogenase type 1, 2, and breast cancer*. *Oncotarget* **8**:30552-30562 https://doi.org/10.18632/oncotarget.15547 | PubMed
25. **Shehu A.,** et al. (2008) Prolactin receptor-associated protein/17beta-hydroxysteroid dehydrogenase type 7 gene (Hsd17b7) plays a crucial role in embryonic development and fetal survival. *Mol Endocrinol* **22**:2268-77 https://doi.org/10.1210/me.2008-0165 | PubMed

26. **Marijanovic Z.,** et al. (2003) Closing the gap: identification of human 3-ketosteroid reductase, the last unknown enzyme of mammalian cholesterol biosynthesis. *Mol Endocrinol* **17**:1715-25 https://doi.org/10.1210/me.2002-0436 | PubMed

27. **Jan T.A.,** et al. (2021) Spatiotemporal dynamics of inner ear sensory and non-sensory cells revealed by single-cell transcriptomics. *Cell Rep* **36**:109358 https://doi.org/10.1016/j.celrep.2021.109358 | PubMed

28. **Qian F.,** et al. (2022) Single-cell RNA-sequencing of zebrafish hair cells reveals novel genes potentially involved in hearing loss. *Cell Mol Life Sci* **79**:385 https://doi.org/10.1007/s00018-022-04410-2 | PubMed

29. **Maeda R.,** et al. (2017) Functional Analysis of the Transmembrane and Cytoplasmic Domains of Pcdh15a in Zebrafish Hair Cells. *J Neurosci* **37**:3231-3245 https://doi.org/10.1523/jneurosci.2216-16.2017 | PubMed

30. **Kindt K.S.,** Finch G., Nicolson T. (2012) Kinocilia mediate mechanosensitivity in developing zebrafish hair cells. *Dev Cell* **23**:329-41 https://doi.org/10.1016/j.devcel.2012.05.022 | PubMed

31. **Burns J.C.,** et al. (2015) Single-cell RNA-Seq resolves cellular complexity in sensory organs from the neonatal inner ear. *Nat Commun* **6**:8557 https://doi.org/10.1038/ncomms9557 | PubMed

32. **Xu Z.,** et al. (2022) Profiling mouse cochlear cell maturation using 10× Genomics single-cell transcriptomics. *Front Cell Neurosci* **16**:962106 https://doi.org/10.3389/fncel.2022.962106 | PubMed

33. **Wilkerson B.A.,** et al. (2021) Novel cell types and developmental lineages revealed by single-cell RNA-seq analysis of the mouse crista ampullaris. *eLife* **10** https://doi.org/10.7554/elife.60108 | PubMed

34. **Yang Q.,** et al. (2017) Behavioral methods for the functional assessment of hair cells in zebrafish. *Front Med* **11**:178-190 https://doi.org/10.1007/s11684-017-0507-x | PubMed

35. **Xiao T.,** et al. (2005) A GFP-based genetic screen reveals mutations that disrupt the architecture of the zebrafish retinotectal projection. *Development* **132**:2955-67 https://doi.org/10.1242/dev.01861 | PubMed

36. **Crumling M.A.,** et al. (2012) Hearing loss and hair cell death in mice given the cholesterol-chelating agent hydroxypropyl-β-cyclodextrin. *PLoS One* **7**:e53280 https://doi.org/10.1371/journal.pone.0053280 | PubMed

37. **Gao G.,** et al. (2022) Kiaa1024L/Minar2 is essential for hearing by regulating cholesterol distribution in hair bundles. *eLife* 11 https://doi.org/10.7554/elife.80865 | PubMed

38. **Schoop V.,** et al. (2021) Cellular cholesterol and how to find it. *Biochim Biophys Acta Mol Cell Biol Lipids* **1866**:158989 https://doi.org/10.1016/j.bbalip.2021.158989 | PubMed

39. **Cheng H.,** et al. (2025) GDC: Integration of Multi-Omic and Phenotypic Resources to Unravel the Genetic Pathogenesis of Hearing Loss. *Adv Sci (Weinh)* e2408891 https://doi.org/10.1002/advs.202408891 | PubMed

40. **Lev S** (2012) Nonvesicular lipid transfer from the endoplasmic reticulum. *Cold Spring Harb Perspect Biol* **4** https://doi.org/10.1101/cshperspect.a013300 | PubMed

41. **Stevenson J.,** Huang E.Y., Olzmann J.A. (2016) Endoplasmic Reticulum-Associated Degradation and Lipid Homeostasis. *Annu Rev Nutr* **36**:511-42 https://doi.org/10.1146/annurev-nutr-071715-051030 | PubMed

42. **Yamasaki A.,** et al. (2014) Rer1p regulates the ER retention of immature rhodopsin and modulates its intracellular trafficking. *Sci Rep* **4**:5973 https://doi.org/10.1038/srep05973 | PubMed

43. **Kaether C.,** et al. (2007) Endoplasmic reticulum retention of the gamma-secretase complex component Pen2 by Rer1. *EMBO Rep* **8**:743-8 https://doi.org/10.1038/sj.embor.7401027 | PubMed

44. **Duan W.R.,** Linzer D.I., Gibori G. (1996) Cloning and characterization of an ovarian-specific protein that associates with the short form of the prolactin receptor. *J Biol Chem* **271**:15602-7 https://doi.org/10.1074/jbc.271.26.15602 | PubMed

45. **Nokelainen P.,** et al. (1998) Expression cloning of a novel estrogenic mouse 17 beta-hydroxysteroid dehydrogenase/17-ketosteroid reductase (m17HSD7), previously described as a prolactin receptor-associated protein (PRAP) in rat. *Mol Endocrinol* **12**:1048-59 https://doi.org/10.1210/mend.12.7.0134 | PubMed

46. **Törn S.,** et al. (2003) Production, purification, and functional analysis of recombinant human and mouse 17beta-hydroxysteroid dehydrogenase type 7. *Biochem Biophys Res Commun* **305**:37-45 https://doi.org/10.1016/s0006-291x(03)00694-6 | PubMed

47. **Ohnesorg T.,** et al. (2006) Transcriptional regulation of human and murine 17beta-hydroxysteroid dehydrogenase type-7 confers its participation in cholesterol biosynthesis. *J Mol Endocrinol* **37**:185-97 https://doi.org/10.1677/jme.1.02043 | PubMed

48. **Seth G.,** McIvor R.S., Hu W.S. (2006) 17Beta-hydroxysteroid dehydrogenase type 7 (Hsd17b7) reverts cholesterol auxotrophy in NS0 cells. *J Biotechnol* **121**:241-52 https://doi.org/10.1016/j.jbiotec.2005.07.017 | PubMed

49. **Ohnesorg T.,** Adamski J. (2006) Analysis of the 5' flanking regions of human and murine HSD17B7: identification of a cholesterol dependent enhancer region. *Mol Cell Endocrinol* **248**:164-7 https://doi.org/10.1016/j.mce.2005.10.016 | PubMed

50. **Krazeisen A.,** et al. (1999) Determination of cDNA, gene structure and chromosomal localization of the novel human 17beta-hydroxysteroid dehydrogenase type 7(1). *FEBS Lett* **460**:373-9 https://doi.org/10.1016/s0014-5793(99)01366-6 | PubMed

51. **Plourde M.,** et al. (2009) *Analysis of 17beta-hydroxysteroid* dehydrogenase types 5, 7, and 12 genetic sequence variants in breast cancer cases from French Canadian Families with high risk of breast and ovarian cancer. *J Steroid Biochem Mol Biol* **116**:134-53 https://doi.org/10.1016/j.jsbmb.2009.05.005 | PubMed

52. **Song D.,** et al. (2006) Expression of aromatase and 17beta-hydroxysteroid dehydrogenase types 1, 7 and 12 in breast cancer. An immunocytochemical study. *J Steroid Biochem Mol Biol* **101**:136-44 https://doi.org/10.1016/j.jsbmb.2006.06.015 | PubMed

53. **Wang X.Q.,** et al. (2017) Inhibition of 17beta-hydroxysteroid dehydrogenase type 7 modulates breast cancer protein profile and enhances apoptosis by down-regulating GRP78. *J Steroid Biochem Mol Biol* **172**:188-197 https://doi.org/10.1016/j.jsbmb.2017.06.009 | PubMed

54. **Wang X.,** et al. (2015) Synergistic control of sex hormones by 17β-HSD type 7: a novel target for estrogen-dependent breast cancer. *J Mol Cell Biol* **7**:568-79 https://doi.org/10.1093/jmcb/mjv028 | PubMed

55. **Sang X.,** et al. (2019) Mutual regulations and breast cancer cell control by steroidogenic enzymes: Dual sex-hormone receptor modulation upon 17β-HSD7 inhibition. *J Steroid Biochem Mol Biol* **193**:105411 https://doi.org/10.1016/j.jsbmb.2019.105411 | PubMed

56. **Maxfield F.R.,** van Meer G. (2010) Cholesterol, the central lipid of mammalian cells. *Curr Opin Cell Biol* **22**:422-9 https://doi.org/10.1016/j.ceb.2010.05.004 | PubMed

57. **Subczynski W.K.,** et al. (2017) High Cholesterol/Low Cholesterol: Effects in Biological Membranes: A Review. *Cell Biochem Biophys* **75**:369-385 https://doi.org/10.1007/s12013-017-0792-7 | PubMed

58. **Takahashi S.,** et al. (2016) Susceptibility of outer hair cells to cholesterol chelator 2-hydroxypropyl-β-cyclodextrine is prestin-dependent. *Sci Rep* **6**:21973 https://doi.org/10.1038/srep21973 | PubMed

59. **Thoenes M.,** et al. (2015) OSBPL2 encodes a protein of inner and outer hair cell stereocilia and is mutated in autosomal dominant hearing loss (DFNA67). *Orphanet J Rare Dis* **10**:15 https://doi.org/10.1186/s13023-015-0238-5 | PubMed

60. **Zalewski C.K.,** et al. (2021) Auditory phenotype of Smith-Lemli-Opitz syndrome. *Am J Med Genet A* **185**:1131-1141 https://doi.org/10.1002/ajmg.a.62087 | PubMed

61. **Forge A.,** Davies S., Zajic G. (1988) Characteristics of the membrane of the stereocilia and cell apex in cochlear hair cells. *J Neurocytol* **17**:325-34 https://doi.org/10.1007/bf01187855 | PubMed

62. **Chakraborty S.,** et al. (2020) How cholesterol stiffens unsaturated lipid membranes. *Proc Natl Acad Sci U S A* **117**:21896-21905 https://doi.org/10.1073/pnas.2004807117 | PubMed

63. **Powers R.J.,** et al. (2014) The local forces acting on the mechanotransduction channel in hair cell stereocilia. *Biophys J* **106**:2519-28 https://doi.org/10.1016/j.bpj.2014.03.034 | PubMed

64. **Powers R.J.,** et al. (2012) Stereocilia membrane deformation: implications for the gating spring and mechanotransduction channel. *Biophys J* **102**:201-10 https://doi.org/10.1016/j.bpj.2011.12.022 | PubMed

65. **Jeong H.,** et al. (2022) Structures of the TMC-1 complex illuminate mechanosensory transduction. *Nature* **610**:796-803 https://doi.org/10.1038/s41586-022-05314-8 | PubMed

66. **Clark S.,** et al. (2024) The structure of the Caenorhabditis elegans TMC-2 complex suggests roles of lipid-mediated subunit contacts in mechanosensory transduction. *Proc Natl Acad Sci U S A* **121**:e2314096121 https://doi.org/10.1073/pnas.2314096121 | PubMed

67. **Zhao Y.,** et al. (2014) A novel DFNA36 mutation in TMC1 orthologous to the Beethoven (Bth) mouse associated with autosomal dominant hearing loss in a Chinese family. *PLoS One* **9**:e97064 https://doi.org/10.1371/journal.pone.0097064 | PubMed

68. **Hildebrand M.S.,** et al. (2011) DFNA8/12 caused by TECTA mutations is the most identified subtype of nonsyndromic autosomal dominant hearing loss. *Hum Mutat* **32**:825-34 https://doi.org/10.1002/humu.21512 | PubMed

69. **Vahava O.,** et al. (1998) Mutation in transcription factor POU4F3 associated with inherited progressive hearing loss in humans. *Science* **279**:1950-4 https://doi.org/10.1126/science.279.5358.1950 | PubMed

70. **Guan J.,** et al. (2020) Recurrent de novo WFS1 pathogenic variants in Chinese sporadic patients with nonsyndromic sensorineural hearing loss. *Mol Genet Genomic Med* **8**:e1367 https://doi.org/10.1002/mgg3.1367 | PubMed

71. **Zhao J.,** et al. (2022) Mutation analysis of the WFS1 gene in a Chinese family with autosomal-dominant non-syndrome deafness. *Sci Rep* **12**:22180 https://doi.org/10.1038/s41598-022-26850-3 | PubMed

72. **Tian T.,** et al. (2018) Identification of a novel MYO6 mutation associated with autosomal dominant non-syndromic hearing loss in a Chinese family by whole-exome sequencing. *Genes Genet Syst* **93**:171-179 https://doi.org/10.1266/ggs.18-00006 | PubMed

73. **Li Q.,** et al. (2021) A novel KCNQ4 gene variant (c.857A>G; p.Tyr286Cys) in an extended family with non-syndromic deafness 2A. *Mol Med Rep* **23** https://doi.org/10.3892/mmr.2021.12059 | PubMed

74. **Mi Y.,** et al. (2021) Early truncation of the N-terminal variable region of EYA4 gene causes dominant hearing loss without cardiac phenotype. *Mol Genet Genomic Med* **9**:e1569 https://doi.org/10.1002/mgg3.1569 | PubMed

75. **Kubisch C.,** et al. (1999) KCNQ4, a novel potassium channel expressed in sensory outer hair cells, is mutated in dominant deafness. *Cell* **96**:437-46 https://doi.org/10.1016/s0092-8674(00)80556-5 | PubMed

76. **Mencía A.,** et al. (2008) A novel KCNQ4 pore-region mutation (p.G296S) causes deafness by impairing cell-surface channel expression. *Hum Genet* **123**:41-53 https://doi.org/10.1007/s00439-007-0447-7 | PubMed

77. **Zhang J.,** Scherer S.S., Yum S.W. (2011) Dominant Cx26 mutants associated with hearing loss have dominant-negative effects on wild type Cx26. *Mol Cell Neurosci* **47**:71-8 https://doi.org/10.1016/j.mcn.2010.10.002 | PubMed

78. **Morell R.J.,** et al. (2000) A new locus for late-onset, progressive, hereditary hearing loss DFNA20 maps to 17q25. *Genomics* **63**:1-6 https://doi.org/10.1006/geno.1999.6058 | PubMed

79. **Jokela H.,** et al. (2010) Hydroxysteroid (17beta) dehydrogenase 7 activity is essential for fetal de novo cholesterol synthesis and for neuroectodermal survival and cardiovascular differentiation in early mouse embryos. *Endocrinology* **151**:1884-92 https://doi.org/10.1210/en.2009-0928 | PubMed

80. **Wei G.,** et al. (2022) Dual-Specificity Phosphatase 14 Regulates Zebrafish Hair Cell Formation Through Activation of p38 Signaling Pathway. *Front Cell Neurosci* **16**:840143 https://doi.org/10.3389/fncel.2022.840143 | PubMed

81. **Kimmel C.B.,** et al. (1995) Stages of embryonic development of the zebrafish. *Dev Dyn* **203**:253-310 https://doi.org/10.1002/aja.1002030302 | PubMed

82. **Ratnadiwakara M.,** Anko M.L. (2018) mRNA Stability Assay Using transcription inhibition by Actinomycin D in Mouse Pluripotent Stem Cells. *Bio Protoc* **8**:e3072 https://doi.org/10.21769/bioprotoc.3072 | PubMed

83. **Meyers J.R.,** et al. (2003) Lighting up the senses: FM1-43 loading of sensory cells through nonselective ion channels. *J Neurosci* **23**:4054-65 https://doi.org/10.1523/jneurosci.23-10-04054.2003 | PubMed

84. **Lai T.W.,** et al. (2022) Cichoric Acid May Play a Role in Protecting Hair Cells from Ototoxic Drugs. *Int J Mol Sci* **23** https://doi.org/10.3390/ijms23126701 | PubMed

85. **Gong J.,** et al. (2021) Claudin h Is Essential for Hair Cell Morphogenesis and Auditory Function in Zebrafish. *Front Cell Dev Biol* **9**:663995 https://doi.org/10.3389/fcell.2021.663995 | PubMed

86. **Huang da W.,** Sherman B.T., Lempicki R.A. (2009) Systematic and integrative analysis of large gene lists using DAVID bioinformatics resources. *Nat Protoc* **4**:44-57 https://doi.org/10.1038/nprot.2008.211 | PubMed

87. **Stuart T.,** et al. (2019) Comprehensive Integration of Single-Cell Data. *Cell* **177**:1888-1902. https://doi.org/10.1016/j.cell.2019.05.031 | PubMed

88. **Yu G.,** et al. (2012) clusterProfiler: an R package for comparing biological themes among gene clusters. *Omics* **16**:284-7 https://doi.org/10.1089/omi.2011.0118 | PubMed

Peer reviews

Reviewer #1 (Public review):

Summary:

This study identifies HSD17B7 as a cholesterol biosynthesis gene enriched in sensory hair cells, with demonstrated importance for auditory behavior and potential involvement in mechanotransduction. Using zebrafish knockdown and rescue experiments, the authors show that loss of hsd17b7 reduces cholesterol levels and impairs hearing behavior. They also report a heterozygous nonsense variant in a patient with hearing loss. The gene mutation has a complex and somewhat inconsistent phenotype, appearing to mislocalize, reduce mRNA and protein levels, and alter cholesterol distribution, supporting HSD17B7 as a potential deafness gene.

The study presents an interesting deafness candidate with a complex mechanism, and highlights an underexplored role for cholesterol (and lipids) in hair cell function.

The authors were very responsive to the initial reviews, and the manuscript is now significantly stronger.

Strengths:

- HSD17B7 is a new candidate deafness gene with plausible biological relevance.

- Cross-species RNAseq convincingly shows hair-cell enrichment.

- Lipid metabolism, particularly cholesterol homeostasis, is an emerging area of interest in auditory function.

- The connection between cholesterol levels and MET is potentially impactful and, if substantiated, would represent a significant advance.

- The localization of HSD17B7 is reasonably convincing, despite the lack of a KO control: In HEI-OC1 cells, HSD17B7 localizes to the ER, as expected. In mouse hair cells, the staining pattern is cytosolic. The developmental increase between P1 and P4, and the higher expression in OHCs aligns nicely with RNAseq data.

Weaknesses:

- The pathogenic mechanism of the E182STOP variant is unclear: The mutant protein presumably does not affect WT protein localization, arguing against a dominant-negative effect. Yet, overexpression of HSD17B7-E182* alone causes toxicity in zebrafish and it binds and mislocalizes cholesterol in HEI-OC1 cells, suggesting some gain-of-function or toxic effect. In addition, the mRNA of the variant has low expression level, suggesting nonsense-mediated decay. The mechanistic conclusions of the study are therefore not as clear cut as one would had hoped, but it might just be a reflection of real biological complexity.

- The link to human deafness is based on a single heterozygous patient with no syndromic features. Given that nearly all known cholesterol metabolism disorders are syndromic, this raises concerns about causality or specificity. HSD17B7 is therefore, at this point, a candidate deafness gene, and not a fully established "novel deafness gene". This is acknowledged by the authors.

- This study does not directly investigate how reduced cholesterol levels affect MET. However, this is not a significant limitation given the study's scope, and it is reasonable that such detailed functional analyses are left to specialists in hair cell physiology.

https://doi.org/10.7554/eLife.108108.2.sa2

Reviewer #2 (Public review):

A summary of what the authors were trying to achieve.

The authors aim to determine whether the gene Hsb17b7 is essential for hair cell function and, if so, to elucidate the underlying mechanism, specifically the HSB17B7 metabolic role in cholesterol biogenesis. They use animal, tissue, or data from zebrafish, mouse, and human patients.

Strengths:

(1) This is the first study of Hsb17b7 in the zebrafish (a previous report identified this gene as a hair cell marker in the mouse utricle).

(2) The authors demonstrate that Hsb17b7 is expressed in hair cells of zebrafish and the mouse cochlea.

(3) In zebrafish larvae, a likely KO of the Hsb17b7 gene causes a mild phenotype in an acoustic/vibrational assay, which also involves a motor response.

(4) In zebrafish larvae, a likely KO of the Hsb17b7 gene causes a mild reduction in lateral line neuromast hair cell number and a mild decrease in the overall mechanotransduction activity of hair cells, assayed with a fluorescent dye entering the mechanotransduction channels.

(5) When HSB17B7 is overexpressed in a cell line, it goes to the ER, and an increase in Cholesterol cytoplasmic puncta is detected. Instead, when a truncated version of HSB17B7 is overexpressed, HSB17B7 forms aggregates that co-localize with cholesterol.

(6) It seems that the level of cholesterol in crista and neuromast hair cells decreases when Hsb17b7 is defective

Comments on the revised version:

Overall, the paper has been improved, but it still needs to be moderated regarding the observed effects and their qualification. I suggest expressing each effect as % {plus minus} SD and indicating it in the main text to inform the reader.

- The title " HSD17B7 is required for the function of sensory hair cells by regulating cholesterol Synthesis" should be moderated: "affects" instead of "required" would be better.

- In the abstract "conserved and essential role for HSD17B7-mediated cholesterol biosynthesis", the term essential seems overstated and premature

- In the discussion: "Collectively, these results suggest that the heterozygous c.544G>T (p.E182*) variant contributes to auditory dysfunction through potential pathogenic mechanisms: haploinsufficiency caused by reduced"...; "could contribute" would be safer.

- In the discussion: "In summary, our study identifies HSD17B7 as a critical regulator of cholesterol synthesis in sensory hair cells and as an essential factor in normal MET and sound-evoked sensory responses. "This part is still an overstatement. The effect in zebrafish is not directly shown to affect hearing, and startle reflex impairment is mild. It is not essential.

https://doi.org/10.7554/eLife.108108.2.sa1

Author response:

The following is the authors' response to the original reviews.

> ***Public Reviews:***
>
> ***Reviewer #1 (Public review):***
>
> *(1) The pathogenic mechanism of the E182STOP variant is unclear. The mutant protein does not appear to affect WT protein localization, arguing against a dominant-negative effect. Yet, overexpression of HSD17B7-E182* alone causes toxicity in zebrafish and mislocalizes cholesterol in HEI-OC1 cells, suggesting a gain-of-function or toxic effect. In addition, the variant mRNA is expressed at a low level, consistent with nonsense-mediated decay. This apparent complexity and inconsistency need clearer explanation.*

We appreciate the reviewer's careful evaluation of this mechanistic complexity. Based on our combined molecular, cellular, and *in vivo* data, we propose that the pathogenic effect of the HSD17B7-E182* variant reflects a composite mechanism, rather than a classical dominant-negative effect.

At the transcript level, the E182* variant introduces a premature termination codon and shows markedly reduced mRNA abundance, consistent with partial degradation by nonsense-mediated mRNA decay. This reduction is expected to decrease overall HSD17B7 dosage, contributing a loss-of-function component. Unlike HSD17B7, the truncated HSD17B7^{E182*} mislocalizes cholesterol in HEI-OC1 cells, and overexpression alone reduces hair cell MET function and startle response in zebrafish embryos. We therefore propose that the truncated protein disturbing local cholesterol homeostasis, thereby exerts a toxic or ectopic gain-of-function.

We have revised the manuscript to clarify the dual-mechanism model.

> *(2) The link to human deafness is based on a single heterozygous patient with no syndromic features. Given that nearly all known cholesterol metabolism disorders are syndromic, this raises concerns about causality or specificity. The term "novel deafness gene" is premature without additional cases or segregation data.*

We thank the reviewer for this important point. We fully agree that, based on a single heterozygous case without segregation data, it is premature to designate HSD17B7 as a novel deafness gene. Therefore, we have revised the manuscript to use the description of "candidate deafness genes".

> *(3) The localization of HSD17B7 should be clarified better: In HEI-OC1 cells, HSD17B7 localizes to the ER, as expected. In mouse hair cells, the staining pattern is cytosolic and almost perfectly overlaps with the hair cell marker used, Myo7a. This needs to be discussed. Without KO tissue, HSD17B7 antibody specificity remains uncertain.*

We thank the reviewer for the constructive comments regarding HSD17B7 localization and antibody specificity.

Regarding subcellular localization, the original Figure 1K was intended to demonstrate the expression of HSD17B7 in mouse hair cells. To address this concern, we performed additional immunostaining on dissected organ of Corti sections at P1, P4, and P7 using higher magnification. Using parvalbumin as a hair cell marker, HSD17B7 displayed a partially punctate intracellular pattern in hair cells (revised Figure 1K). This pattern is consistent with localization to membrane-associated compartments, including the endoplasmic reticulum, and agrees with the ER-associated localization observed in HEI-OC1 cells and zebrafish hair cells. In mature hair cells, ER-associated signals may appear cytosolic and overlap with general hair cell markers such as Myo7a.

Regarding antibody specificity, although HSD17B7 knockout tissue was not available, we performed complementary validation experiments in HEI-OC1 cells. Cells were transfected with pCMV-Flag, pCMV-Flag-hHSD17B7WT, or pCMV-hHSD17B7WT-EGFP constructs and stained with anti-Flag, anti-EGFP, and anti-HSD17B7 antibodies. The HSD17B7 antibody signal showed strong co-localization with both FLAG- and EGFP-tagged HSD17B7 (revised Figure S1A and B), supporting its specificity.

> ***Reviewer #2 (Public review):***
>
> *(1) The statement that HSD17B7 is "highly" expressed in sensory hair cells in mice and zebrafish seems incorrect for zebrafish:*
>
> *(a) The data do not support the notion that HSB17B7 is "highly expressed" in zebrafish. Compared to other genes (TMC1, TMIE, and others), the HSB17B7 level of expression in neuromast hair cells is low (Figure 1F), and by extension (Figure 1C), also in all hair cells. This interpretation is in line with the weak detection of an mRNA signal by ISH (Figure 1G I"). On this note, the staining reported in I" does not seem to label the cytoplasm of neuromast hair cells. An antisense probe control, along with a positive control (such as TMC1 or another), is necessary to interpret the ISH signal in the neuromast.*

We thank the reviewer for this detailed evaluation and agree that the description of HSD17B7 expression in zebrafish hair cells requires clarification.

To address this, we performed a quantitative comparison of average expression levels within neuromast hair cells using log-normalized single-cell RNA-seq data. This analysis shows that *hsd17b7* is expressed at a level comparable to several known MET-associated genes (e.g., *tmc1* and *lhfpl5a*) (revised Figure 1D). Regarding the pseudotime heatmap (Figure 1F), we now

state that this analysis illustrates temporal expression dynamics within neuromast hair cell development.

In addition, we have clarified the interpretation of the whole-mount *in situ* hybridization data by emphasizing that the signal indicates spatial enrichment rather than high transcript abundance.

We have updated the figure panels, legends, and corresponding text in the Results section to reflect these changes.

> *(b) However, this is correct for mouse cochlear hair cells, based on single-cell RNA-seq published databases and immunostaining performed in the study. However, the specificity of the anti-HSD17B7 antibody used in the study (in immunostaining and western blot) is not demonstrated. Additionally, it stains some supporting cells or nerve terminals. Was that expression expected?*

To assess antibody specificity, we performed validation experiments using distinct epitopes. In HEI-OC1 cells transfected with pCMV-Flag-HSD17B7, or pCMV-HSD17B7-EGFP constructs, immunostaining with anti-HSD17B7 showed strong co-localization with both FLAG- and EGFP-tag (revised Figure S1B). In addition, western blot analyses using the same constructs confirmed the specific detection of HSD17B7 protein (revised Figure S1B). These validation data have now been included as supplementary figures in the revised manuscript and provide independent supporting evidence for the specificity of the anti-HSD17B7 antibody.

> *(2) A previous report showed that HSD17B7 is expressed in mouse vestibular hair cells by single-cell RNAseq and immunostaining in mice, but it is not cited: Spatiotemporal dynamics of inner ear sensory and non-sensory cells revealed by single-cell transcriptomics. Jan TA, Eltawil Y, Ling AH, Chen L, Ellwanger DC, Heller S, Cheng AG. Cell Rep. 2021 Jul 13;36(2):109358. doi: 10.1016/j.celrep.2021.109358.*

We have now cited this reference in the revised manuscript.

> *(3) Overexpressed HSD17B7-EGFP C-terminal fusion in zebrafish hair cells shows a punctiform signal in the soma but apparently does not stain the hair bundles. One limitation is the consequence of the C-terminal EGFP fusion to HSD17B7 on its function, which is not discussed.*

We thank the reviewer for raising this important technical point. The apparent absence of an HSD17B7-EGFP signal in hair bundles is primarily due to the imaging strategy and the selection of representative images. In zebrafish hair cells, the EGFP signal within hair bundles is extremely strong. To better visualize the intracellular distribution of HSD17B7 within the hair cell soma, we selected representative confocal optical sections that were focused on the cell body rather than on the apical hair bundle plane. As a result, the hair bundle signal is not visible in the images shown.

Importantly, we agree that C-terminal EGFP fusion may potentially influence protein localization or function. We have therefore revised the Discussion to discuss this limitation and to clarify that our central conclusions regarding HSD17B7 function are primarily supported by loss-of-function analyses, rescue experiments using untagged mRNA, and cholesterol perturbation phenotypes, rather than relying solely on EGFP-tagged overexpression constructs.

> *(4) A mutant Zebrafish CRISPR was generated, leading to a truncation after the first 96 aa out of the 340 aa total. It is unclear why the gene editing was not done closer to the ATG. This allele may conserve some function, which is not discussed.*

Targeting regions close to the ATG is indeed a commonly used strategy for CRISPR-mediated gene disruption. In this study, sgRNA selection was guided by online CRISPR design tools (CRISPRscan), prioritizing predicted cutting efficiency and specificity. This strategy resulted in a frameshift mutation introducing a premature stop codon after amino acid 96 of the 340-aa Hsd17b7 protein.

Importantly, this truncation removes most of the conserved catalytic core required for 17β-hydroxysteroid dehydrogenase activity, including key motifs involved in NAD(P)-binding and substrate recognition. Therefore, although the mutation does not occur immediately adjacent to the ATG, the resulting allele is predicted to lack enzymatic function. We have clarified this rationale and discussed the functional consequences of the truncation in the revised manuscript.

> *(5) The hsd17b7 mutant allele has a slightly reduced number of genetically labeled hair cells (quantified as a 16% reduction, estimated at 1-2 HC of the 9 HC present per neuromast). On a note, it is unclear what criteria were used to select HC in the picture. Some Brn3C:mGFP positive cells are apparently not included in the quantifications (Figure 2F, Figure 5A).*

Upon re-evaluation, we recognized that the original figure annotations were not sufficiently clear and may have led to confusion regarding hair cell selection. In the original images, the absence of dashed outlines around some Brn3c:mGFP$^+$ cells may have been misinterpreted as their exclusion from analysis. To address this issue, we have revised Figures 2F and 5A by updating the annotations to ensure that all Brn3c:mGFP$^+$ hair cells within each neuromast are clearly visible and unambiguously included (revised Figures 2F and 6A). Corresponding figure legends have also been revised to clarify the criteria used for hair cell identification and quantification.

> *(6) The authors used FM4-64 staining to evaluate the hair cell mechanotransduction activity indirectly. They found a 40% reduction in labeling intensity in the HCs of the lateral line neuromast. Because the reduction of hair cell number (16%) is inferior to the reduction of FM4-64 staining, the authors argue that it indicates that the defect is primarily affecting the mechanotransduction function rather than the number of HCs. This argument is insufficient. Indeed, a scenario could be that some HC cells died and have been eliminated, while others are also engaged in this path and no longer perform the MET function. The numbers would then match. If single-cell staining can be resolved, one could determine the FM4-64 intensity per cell. It would also be informative to evaluate the potential occurrence of cell death in this mutant. On another note, the current quantification of the FM4-64 fluorescence intensity and its normalization are not described in the methods. More importantly, an independent and more direct experimental assay is needed to confirm this point. For example, using a GCaMP6-T2A-RFP allele for Ca2+ imaging and signal normalization.*

We have revised the FM4-64 quantification strategy. Instead of measuring fluorescence intensity at the neuromast level, FM4-64 uptake was re-quantified at the single hair cell level. Hair cells within each neuromast were identified based on mGFP labeling, and the mean FM4-64 fluorescence intensity was measured for each individual hair cell. The average FM4-64 intensity per hair cell was then calculated for each neuromast and used for group comparisons (revised Figures 2F, 6B, and 8B, Figure S5B). The updated quantification method, normalization procedure, and analysis pipeline have now been described in the revised Methods section.

As supportive evidence, we further analyzed single-cell RNA-seq data from control and *hsd17b7* mutant hair cells (revised Figure 3). This analysis revealed dysregulation of multiple genes involved in the MET machinery, including reduced expression of tip-link–associated

components and altered expression of other MET-related genes. While these transcriptional changes do not constitute a direct functional assay, they are consistent with perturbation of MET-associated pathways and complement the FM4-64 findings.

> *(7) The authors used an acoustic startle response to elicit a behavioral response from the larvae and evaluate the "auditory response". They found a significative decrease in the response (movement trajectory, swimming velocity, distance) in the hsd17b7 mutant. The authors conclude that this gene is crucial for the "auditory function in zebrafish".*
>
> *This is an overstatement:*
>
> *(a) First, this test is adequate as a screening tool to identify animals that have lost completely the behavioral response to this acoustic and vibrational stimulation, which also involves a motor response. However, additional tests are required to confirm an auditory origin of the defect, such as Auditory Evoked Potential recordings, or for the vestibular function, the Vestibulo-Ocular Reflex.*

We thank the reviewer for highlighting the limitations in interpreting the acoustic startle assay. We have revised the manuscript to avoid overstatement and now describe the observed phenotype as a reduction in the behavioral response to acoustic and vibrational stimulation, rather than concluding a specific impairment of auditory function.

> *(b) Secondly, the behavioral defects observed in the mutant compared to the control are significantly different, but the differences are slight, contained within the Standard Deviation (20% for velocity, 25% for distance). To this point, the Figure 2 B and C plots are misleading because their y-axis do not start at 0.*

We have corrected Figures 2B and 2C so that the y-axes start at zero, thereby providing a more transparent visualization of the behavioral differences. The figure legends have also been revised to clarify the presentation of the data.

> *(8) Overexpression of HSD17B7 in cell line HEI-OC1 apparently "significantly increases" the intensity of cholesterol-related signal using a genetically encoded fluorescent sensor (D4H-mCherry). However, the description of this quantification (per cell or per surface area) and the normalization of the fluorescent signal are not provided.*

The quantification of the D4H-mCherry signal in HEI-OC1 cells was performed at the single-cell level. Specifically, individual cells were segmented based on morphology, and the mean fluorescence intensity of D4H-mCherry per cell was measured. To account for variability in cell size and imaging conditions, fluorescence intensity was normalized to the background signal measured from cell-free regions in the same field of view. We have now clarified the quantification strategy and normalization procedure in the revised Methods and Results sections.

> *(9) When this experiment is conducted in vivo in zebrafish, a reduction in the "DH4 relative intensity" is detected (same issue with the absence of a detailed method description). However, as the difference is smaller than the standard deviation, this raises questions about the biological relevance of this result.*

We have now clarified the quantification strategy and normalization procedure in the revised Methods and Results sections.

> *(10) The authors identified a deaf child as a carrier of a nonsense mutation in HSB17B7, which is predicted to terminate the HSB17B7 protein before the transmembrane domain. However, as no genetic linkage is possible, the causality is not demonstrated.*

We thank the reviewer for raising this important point. Unfortunately, we were unable to obtain the parents' genetic testing data to perform formal genetic and linkage analysis. To

address this limitation, we have revised the manuscript to avoid causal overstatement and now describe the HSD17B7 E182* variant as a candidate pathogenic variant associated with hearing loss. Importantly, our functional analyses in zebrafish and cell-based systems demonstrate that the E182* truncation abolishes key biological activities of HSD17B7, including subcellular localization, cholesterol regulation, mechanotransduction-related activity, and behavioral responses. These convergent functional data provide biological support for the potential pathogenic relevance of this variant.

> *(11) Previous results obtained from mouse HSD17B7-KO (citation below) are not described in sufficient detail. This is critical because, in this paper, the mouse loss-of-function of HSD17B7 is embryonically lethal, whereas no apparent phenotype was reported in heterozygotes, which are viable and fertile. Therefore, it seems unlikely that heterozygous mice exhibit hearing loss or vestibular defects; however, it would be essential to verify this to support the notion that the truncated allele found in one patient is causal.*
>
> *Hydroxysteroid (17beta) dehydrogenase 7 activity is essential for fetal de novo cholesterol synthesis and for neuroectodermal survival and cardiovascular differentiation in early mouse embryos.*
>
> *Jokela H, Rantakari P, Lamminen T, Strauss L, Ola R, Mutka AL, Gylling H, Miettinen T,*
>
> *Pakarinen P, Sainio K, Poutanen M. Endocrinology. 2010 Apr;151(4):1884-92. doi: 10.1210/en.2009-0928. Epub 2010 Feb 25.*

We thank the reviewer for raising this important point. We acknowledge that previous work has shown that complete loss of Hsd17b7 in mice is embryonically lethal, whereas heterozygous animals are viable and fertile (Jokela et al., 2010). Notably, this study primarily focused on embryonic development, cholesterol metabolism, and cardiovascular and neuroectodermal survival, and auditory or vestibular functions were not specifically examined. Therefore, subtle or sensory organ–specific phenotypes in heterozygous mice cannot be excluded.

The human variant identified in this study (E182*) is a nonsense mutation predicted to truncate the HSD17B7 protein prior to the transmembrane and cytoplasmic domains. We therefore present it as a candidate loss-of-function variant, providing supportive human genetic evidence that is consistent with our functional analyses in zebrafish hair cells, rather than as definitive proof of causality. We have revised the manuscript to clarify these points and to acknowledge this limitation.

> *(12) The authors used this truncated protein in their startle response and FM4-64 assays. First, they show that contrary to the WT version, this truncated form cannot rescue their phenotypes when overexpressed. Secondly, they tested whether this truncated protein could recapitulate the startle reflex and FM4-64 phenotypes of the mutant allele. At the homozygous level (not mentioned by the way), it can apparently do so to a lesser degree than the previous mutant. Again, the differences are within the Standard Deviation of the averages. The authors conclude that this mutation found in humans has a "negative effect" on hearing, which is again not supported by the data.*

We thank the reviewer for this important comment. We agree that the overexpression strategy employed in this study does not fully replicate the endogenous heterozygous state observed in patients, and that the magnitude of the observed effects varies across samples. Accordingly, our experiments were not intended to demonstrate a definitive causal role of the HSD17B7 ^{E182*} variant in hearing loss.

Instead, the overexpression assays were designed to assess whether the truncated HSD17B7 protein displays abnormal cellular properties and whether its presence can interfere with

processes relevant to hair cell function. Under these conditions, HSD17B7^{E182*} exhibited aberrant subcellular localization, altered intracellular cholesterol distribution, and was associated with reduced FM4-64 uptake and changes in startle-associated behaviors, whereas the wild-type protein did not.

We revised the manuscript to moderate our conclusions. Rather than claim that the E182* mutation has a definitive “negative effect on auditory function,” we now describe it as a functionally compromised allele that disrupts cholesterol distribution and MET-related activity under overexpression conditions, providing mechanistic support consistent with our zebrafish loss-of-function data and the identification of this variant in a patient with hearing loss. In addition, the "negative effect" statement was based on the result that overexpression of the E182* mutation in wild-type embryos caused the compromised MET function and startle response defect.

> *(13) The authors looked at the distribution of the HSB17B7 in a cell line. The WT version goes to the ER, while the truncated one forms aggregates. An interesting experiment consisted of co-expressing both constructs (Figure S6) to see whether the truncated version would mislocalize the WT version, which could be a mechanism for a dominant phenotype. However, this is not the case.*

We thank the reviewer for raising this important point regarding a potential dominant-negative mechanism. Consistent with the reviewer’s interpretation, we found that HSD17B7^{WT} predominantly localizes to the endoplasmic reticulum, whereas the truncated HSD17B7^{E182*} protein forms intracellular aggregates. Importantly, we further observed that the E182* mutation markedly reduces the stability of both HSD17B7 mRNA and protein, resulting in substantially decreased abundance of the truncated protein (Figure S6B–E). As a consequence, the cellular levels of HSD17B7^E182* are abnormally low.

Based on these findings, we consider it unlikely that the E182* variant exerts its effect through interference with the wild-type protein. Our results suggest that the heterozygous c.544G>T (p.E182*) variant contributes to auditory dysfunction through potential pathogenic mechanisms: 1, haploinsufficiency caused by reduced HSD17B7 expression, 2, functional impairment due to altered protein subcellular localization and cholesterol distribution.

We have revised the Results and Discussion sections. Our conclusions now emphasize that the functional impact of this variant is attributable to decreased effective HSD17B7 dosage, consistent with the observed defects in cholesterol synthesis, MET-related activity, and auditory-associated phenotypes in our model.

> *(14) Through mass spectrometry of HSB17B7 proteins in the cell line, they identified a protein involved in ER retention, RER1. By biochemistry and in a cell line, they show that truncated HSB17B7 prevents the interaction with RER1, which would explain the subcellular localization.*

Consistent with the reviewer’s interpretation, wild-type HSD17B7 interacts with RER1, a protein known to participate in ER retention, whereas this interaction is lost in the truncated HSD17B7 variant. We propose that RER1 is an interacting partner of HSD17B7, providing a mechanistic explanation for the protein's subcellular localization.

> *(15) Information and specificity validation of the HSB17B7 antibody are not presented. It seems that it is the same used on mice by IF and on zebrafish by Western. If so, the antibody could be used on zebrafish by IF to localize the endogenous protein (not overexpression as done here). Secondly, the specificity of the antibody should be verified on the mutant allele. That would bring confidence that the staining on the mouse is likely specific.*

We thank the reviewer for raising this important point regarding antibody specificity and validation. Information on the HSD17B7 antibody and its validation has been provided in our response to comment 1, where we described the use of antibodies recognizing different epitopes and the experimental strategies employed to assess specificity (revised Figure S1A and B).

Although the same antibody was used for Western blot analysis in zebrafish samples, its performance in immunofluorescence staining of zebrafish tissues was suboptimal, with relatively high background. For this reason, we did not rely on this antibody for endogenous Hsd17b7 localization in zebrafish by immunofluorescence and instead employed tagged constructs for subcellular localization analyses. This approach provides more reliable and interpretable localization information under the current experimental conditions.

> ***Recommendations for the authors:***
>
> ***Reviewing Editor Comments:***
>
> *Suggested revisions to help improve the study and the eLife Assessment:*
>
> *(1) FM4-64 uptake: Isolate the effect of hair cell loss and MET reduction.*
>
> *(2) Clarify the mechanistic model: Is the mutant protein pathogenic due to toxicity, lack of expression or function, or both? Come up with a clearer causal chain of events.*
>
> *(3) Mouse immunostaining: Validate the HSD17B7 antibody, and since mouse RNAseq data (gEAR database) suggest that HSD17B7 expression increases dramatically between P0-P5, show this developmental progression by immunostaining of the mouse organ of Corti at P0, P3, and P5.*
>
> *(4) The HSD17B7-E182* expression disrupts cholesterol (D4H staining) in OC1 cells. This should also be demonstrated in the mutant zebrafish.*
>
> *(5) Structural modeling of E182* is uninformative; half the protein is absent. This kind of analysis is better suited for missense variants. Suggest removing this analysis.*

We thank the Reviewing Editor for these constructive suggestions. The major points raised here substantially overlap with the concerns raised in the public reviews. In response, we have:

(1) revised FM4-64 quantification and interpretation to better distinguish hair cell loss from MET impairment;

(2) Clarify the mechanistic mode. Mechanistically, the mutation decreases mRNA abundance and significantly reduces protein levels. Moreover, expression of the p.E182* mutation disrupted the interaction between HSD17B7 and the ER retention receptor RER1, leading to aberrant subcellular localization and altered cholesterol distribution, thereby exacerbating HC dysfunction.

(3) provided additional validation of the HSD17B7 antibody using antibodies targeting distinct epitopes, and extended mouse organ of Corti immunostaining to postnatal stages P1, P4, and P7 to demonstrate the developmental upregulation of HSD17B7 expression;

(4) added *in vivo* zebrafish experiments demonstrating that expression of HSD17B7^{E182*} disrupts cholesterol distribution in hair cells, consistent with the effects observed in HEI-OC1 cells using D4H staining;

(5) removed the structural modeling of the E182* variant.

Recommendations for the authors:

The recommendations from Reviewer #1 and Reviewer #2 were carefully considered and addressed. Most of these points overlap with the public reviews and the Reviewing Editor's comments and have been addressed through a revised mechanistic interpretation, additional clarifications in the Methods, more moderate claims regarding auditory function and human genetics, and the removal or revision of potentially misleading analyses. In addition, a number of minor issues were corrected, including missing or incorrect references, repetitive or unclear statements in the Introduction, insufficient methodological details, imprecise terminology, and typographical or formatting errors. Collectively, these revisions improve the clarity, rigor, and transparency of the study without altering its central conclusions.

https://doi.org/10.7554/eLife.108108.2.sa0